

# Review and consensus recommendations on clinical APT-weighted imaging approaches at 3T: Application to brain tumors

Jinyuan Zhou<sup>1</sup>  | Moritz Zaiss<sup>2,3</sup> | Linda Knutsson<sup>1,4,5</sup>  | Phillip Zhe Sun<sup>6</sup>  | Sung Soo Ahn<sup>7</sup> | Silvio Aime<sup>8</sup> | Peter Bachert<sup>9,10</sup> | Jaishri O. Blakeley<sup>11</sup> | Kejia Cai<sup>12</sup> | Michael A. Chappell<sup>13,14</sup> | Min Chen<sup>15</sup> | Daniel F. Gochberg<sup>16,17,18</sup> | Steffen Goerke<sup>9</sup>  | Hye-Young Heo<sup>1</sup>  | Shanshan Jiang<sup>1</sup> | Tao Jin<sup>19</sup>  | Seong-Gi Kim<sup>20</sup> | John Laterra<sup>11,21</sup> | Daniel Paech<sup>22,23</sup>  | Mark D. Pagel<sup>24</sup>  | Ji Eun Park<sup>25</sup> | Ravinder Reddy<sup>26</sup> | Akihiko Sakata<sup>27</sup> | Sabine Sartoretti-Schefer<sup>28</sup> | A. Dean Sherry<sup>29,30</sup> | Seth A. Smith<sup>16,17,31</sup> | Greg J. Stanisz<sup>32</sup> | Pia C. Sundgren<sup>33,34,35</sup> | Osamu Togao<sup>36</sup> | Moriel Vandsburger<sup>37</sup>  | Zhibo Wen<sup>38</sup> | Yin Wu<sup>39</sup>  | Yi Zhang<sup>40</sup>  | Wenzhen Zhu<sup>41</sup> | Zhongliang Zu<sup>16,17</sup>  | Peter C. M. van Zijl<sup>1,5</sup>

<sup>1</sup>Division of MR Research, Department of Radiology, Johns Hopkins University School of Medicine, Baltimore, Maryland, USA

<sup>2</sup>Magnetic Resonance Center, Max Planck Institute for Biological Cybernetics, Tübingen, Germany

<sup>3</sup>Institute of Neuroradiology, University Hospital Erlangen, Friedrich-Alexander Universität Erlangen-Nürnberg, Erlangen, Germany

<sup>4</sup>Department of Medical Radiation Physics, Lund University, Lund, Sweden

<sup>5</sup>F.M. Kirby Research Center for Functional Brain Imaging, Hugo W. Moser Research Institute at Kennedy Krieger, Baltimore, Maryland, USA

<sup>6</sup>Yerkes Imaging Center, Yerkes National Primate Research Center, Emory University, Atlanta, Georgia, USA

<sup>7</sup>Department of Radiology and Research Institute of Radiological Science, Yonsei University College of Medicine, Seoul, South Korea

<sup>8</sup>Molecular Imaging Center, Department of Molecular Biotechnology and Health Sciences, University of Torino, Torino, Italy

<sup>9</sup>Department of Medical Physics in Radiology, German Cancer Research Center, Heidelberg, Germany

<sup>10</sup>Faculty of Physics and Astronomy, University of Heidelberg, Heidelberg, Germany

<sup>11</sup>Department of Neurology, Johns Hopkins University School of Medicine, Baltimore, Maryland, USA

<sup>12</sup>Department of Radiology, University of Illinois at Chicago, Chicago, Illinois, USA

<sup>13</sup>Mental Health and Clinical Neurosciences and Sir Peter Mansfield Imaging Centre, School of Medicine, University of Nottingham, Nottingham, UK

<sup>14</sup>Nottingham Biomedical Research Centre, Queen's Medical Centre, University of Nottingham, Nottingham, UK

<sup>15</sup>Department of Radiology, Beijing Hospital, National Center of Gerontology, Beijing, China

<sup>16</sup>Vanderbilt University Institute of Imaging Science (VUIIS), Vanderbilt University Medical Center, Nashville, Tennessee, USA

<sup>17</sup>Department of Radiology and Radiological Sciences, Vanderbilt University Medical Center, Nashville, Tennessee, USA

<sup>18</sup>Department of Physics, Vanderbilt University, Nashville, Tennessee, USA

<sup>19</sup>Department of Radiology, University of Pittsburgh, Pittsburgh, Pennsylvania, USA

<sup>20</sup>Center for Neuroscience Imaging Research, Institute for Basic Science and Department of Biomedical Engineering, Sungkyunkwan University, Suwon, South Korea

<sup>21</sup>Hugo W. Moser Research Institute at Kennedy Krieger, Baltimore, Maryland, USA

<sup>22</sup>Department of Radiology, German Cancer Research Center, Heidelberg, Germany

<sup>23</sup>Clinic for Neuroradiology, University Hospital Bonn, Bonn, Germany

<sup>24</sup>Department of Cancer Systems Imaging, The University of Texas MD Anderson Cancer Center, Houston, Texas, USA

The CEST 2020 APTw Imaging Subgroup members: Jinyuan Zhou, Moritz Zaiss, Linda Knutsson, Phillip Zhe Sun, and Peter C.M. van Zijl.

This is an open access article under the terms of the Creative Commons Attribution-NonCommercial-NoDerivs License, which permits use and distribution in any medium, provided the original work is properly cited, the use is non-commercial and no modifications or adaptations are made.

© 2022 The Authors. *Magnetic Resonance in Medicine* published by Wiley Periodicals LLC on behalf of International Society for Magnetic Resonance in Medicine.

- <sup>25</sup>Department of Radiology and Research Institute of Radiology, University of Ulsan College of Medicine, Asan Medical Center, Seoul, South Korea
- <sup>26</sup>Center for Advance Metabolic Imaging in Precision Medicine, Department of Radiology, University of Pennsylvania, Philadelphia, Pennsylvania, USA
- <sup>27</sup>Department of Diagnostic Imaging and Nuclear Medicine, Kyoto University Graduate School of Medicine, Kyoto, Japan
- <sup>28</sup>Institute of Radiology, Kantonsspital Winterthur, Winterthur, Switzerland
- <sup>29</sup>Advanced Imaging Research Center and Department of Radiology, University of Texas Southwestern Medical Center, Dallas, Texas, USA
- <sup>30</sup>Department of Chemistry and Biochemistry, University of Texas at Dallas, Richardson, Texas, USA
- <sup>31</sup>Department of Biomedical Engineering, Vanderbilt University, Nashville, Tennessee, USA
- <sup>32</sup>Department of Medical Biophysics, University of Toronto, Toronto, Ontario, Canada
- <sup>33</sup>Department of Diagnostic Radiology/Clinical Sciences Lund, Lund University, Lund, Sweden
- <sup>34</sup>Lund University Bioimaging Center, Lund University, Lund, Sweden
- <sup>35</sup>Department of Medical Imaging and Physiology, Skåne University Hospital, Lund University, Lund, Sweden
- <sup>36</sup>Department of Molecular Imaging and Diagnosis, Graduate School of Medical Sciences, Kyushu University, Fukuoka, Japan
- <sup>37</sup>Department of Bioengineering, U.C. Berkeley, Berkeley, California, USA
- <sup>38</sup>Department of Radiology, Zhujiang Hospital, Southern Medical University, Guangzhou, Guangdong, China
- <sup>39</sup>Paul C. Lauterbur Research Center for Biomedical Imaging, Shenzhen Institute of Advanced Technology, Chinese Academy of Sciences, Shenzhen, Guangdong, China
- <sup>40</sup>Key Laboratory for Biomedical Engineering of Ministry of Education, Department of Biomedical Engineering, College of Biomedical Engineering and Instrument Science, Zhejiang University, Hangzhou, Zhejiang, China
- <sup>41</sup>Department of Radiology, Tongji Hospital of Tongji Medical College, Huazhong University of Science and Technology, Wuhan, Hubei, China

### Correspondence

Jinyuan Zhou, Division of MR Research, Department of Radiology, Johns Hopkins University, 600 N. Wolfe Street, Park 306G, Baltimore, MD 21287, USA.  
Email: [jzhou2@jhmi.edu](mailto:jzhou2@jhmi.edu)

### Funding information

German Research Foundation (DFG), Grant/Award Number: 445704496; National Research Foundation of Korea (NRF), Grant/Award Number: 2014R1A1A1002716; National Institutes of Health, Grant/Award Numbers: P41EB015909, P41EB029460, R01AG069179, R01CA228188, R01EB015032, R37CA248077; Swedish Cancer Society, Grant/Award Numbers: CAN 2015/251, CAN 2018/468, CAN 2018/550; Swedish Research Council, Grant/Award Numbers: 2015-04170, 2019-01162

Amide proton transfer-weighted (APT<sub>w</sub>) MR imaging shows promise as a biomarker of brain tumor status. Currently used APT<sub>w</sub> MRI pulse sequences and protocols vary substantially among different institutes, and there are no agreed-on standards in the imaging community. Therefore, the results acquired from different research centers are difficult to compare, which hampers uniform clinical application and interpretation. This paper reviews current clinical APT<sub>w</sub> imaging approaches and provides a rationale for optimized APT<sub>w</sub> brain tumor imaging at 3 T, including specific recommendations for pulse sequences, acquisition protocols, and data processing methods. We expect that these consensus recommendations will become the first broadly accepted guidelines for APT<sub>w</sub> imaging of brain tumors on 3 T MRI systems from different vendors. This will allow more medical centers to use the same or comparable APT<sub>w</sub> MRI techniques for the detection, characterization, and monitoring of brain tumors, enabling multi-center trials in larger patient cohorts and, ultimately, routine clinical use.

### KEYWORD

APT<sub>w</sub> standardization, APT-weighted imaging, brain tumor, CEST imaging

## 1 | INTRODUCTION

Amide proton transfer-weighted (APT<sub>w</sub>) imaging is a molecular MRI technique that generates image contrast based on endogenous mobile proteins and peptides in tissue.<sup>1,2</sup> As a type of CEST imaging,<sup>3</sup> the principles and applications of APT<sub>w</sub> imaging have been reviewed in several articles.<sup>4–21</sup> Key abbreviations and nomenclatures

used in the field of APT<sub>w</sub> imaging are listed in Table 1. Data from numerous institutions worldwide have demonstrated that APT<sub>w</sub> imaging adds important value to the standard clinical MRI sequences in brain cancer diagnoses, such as the detection and grading of tumors,<sup>22–37</sup> the assessment of treatment effect versus tumor recurrence,<sup>38–45</sup> prognosis related to tumor progression and survival,<sup>46–48</sup> and the identification of genetic markers.<sup>49–56</sup> It is worth mentioning that brain tumor patients require frequent MRI

exams, and the exposure to gadolinium (Gd)-based contrast agents has been indicated as a risk for people with moderate to advanced kidney failure and for Gd deposition in the brain.<sup>57–59</sup> Although promising, there are several remaining challenging issues for clinical APTw imaging.<sup>11–14</sup> These include scanner RF amplifier constraints, specific absorption rate (SAR) limits, low SNR, long scan times, a complicated contrast mechanism with multiple contributions,  $B_1$  inhomogeneity, and the possibility of artifacts because of motion,  $B_0$  inhomogeneity, and lipids.

The most concerning issue from a radiologist's point of view is that APTw signal intensities depend on the APTw pulse sequence features and parameters used, which may lead to differences in image contrast and in interpretation between sites. Currently, there are large variations in parameters used for APTw imaging in the literature and, except for 1 Food and Drug Administration (FDA)-approved product,<sup>60,61</sup> most vendor sequences are available only as "work in progress" (WIP) software (Tables 2 and 3). Differences in data processing strategies have further complicated the reproducibility and comparison of results between centers. Based on its demonstrated ability to enhance diagnostic specificity in brain tumor assessment, there is a need for the clinical APTw imaging community to work together to develop this emerging technology into an optimized, reproducible, and standardized approach.

Toward this goal, the 7th International Workshop on CEST Imaging (2018)<sup>62</sup> featured a special session to discuss standardization involving the 3 main MRI vendors (GE Healthcare, Milwaukee, Wisconsin, USA; Philips Healthcare, Best, Netherlands; Siemens Healthineers, Erlangen, Germany), illustrating its high priority for this community. The organizing committee of the 8th International Workshop on CEST Imaging (2020)<sup>63</sup> established an APTw Imaging Subgroup to evaluate APTw MRI standardization for brain tumor imaging. The purpose of this subgroup was to review the development of clinical APTw imaging techniques on 3 T MRI scanners and, in collaboration with some of the other leading groups in the field, to provide consensus recommendations for APTw imaging of brain tumors. Because different clinical applications may require a different set of parameters for optimal contrast, this work is limited to the currently most-used application of APTw MRI, namely, the diagnosis of brain tumors and only for the field strength commonly applied to brain tumors in the clinical setting, 3 T. Consistent implementation of these recommendations by MRI vendors will allow more medical centers, worldwide, to routinely use this promising technology in their multi-center clinical trials and in daily clinical practice. This will help to ultimately achieve biomarker status for APTw MRI contrast in the assessment of brain tumors at 3 T.

## 2 | BACKGROUND AND THEORY

The basics of APTw imaging have been explained in several previous review articles.<sup>4–21</sup> Briefly, APTw imaging is generally obtained by RF saturation labeling of the water-exchangeable backbone amide proton pool of proteins and peptides, followed by a physical transfer (chemical exchange) of these saturated amide protons to bulk water protons, resulting in a decrease in their magnetization. Theoretically, the CEST effect of amide protons can be expressed in terms of a so-called amide proton transfer ratio (APTR), a formulation that describes the different parameters on which the CEST effect depends. Based on a 2-pool (small solute/amide proton pool, large water proton pool) slow exchange model with a continuous wave (CW) RF saturation, and assuming no direct saturation (DS) effect, this can be expressed as<sup>64–68</sup>:

$$\begin{aligned} APTR &\approx \frac{f_s k_{sw} \alpha}{R_{1w} + f_s k_{sw} \alpha} \left[ 1 - e^{-(R_{1w} + f_s k_{sw} \alpha) T_{sat}} \right] \\ &\approx \frac{f_s k_{sw} \alpha}{R_{1w}} (1 - e^{-R_{1w} T_{sat}}), \end{aligned} \quad (1)$$

where  $k_{sw}$  is the solute-proton to water-proton exchange rate (tens to hundreds of Hz),  $\alpha$  is the solute proton saturation efficiency,  $f_s$  is the solute proton population fraction ( $f_s = [\text{amide proton}]/[\text{water proton}]$ ,  $[\text{water proton}] = 2 \times 55.6 \text{ M}$ ),  $R_{1w}$  is the longitudinal relaxation rate of water ( $R_{1w} = 1/T_{1w}$ ), and  $T_{sat}$  is the total RF saturation time (Table 1). It is important to note that Equation (1) is an idealized expression under several assumptions, and a more realistic theory must be considered for interpretation of in vivo effects.<sup>65–68</sup> For instance, Equation (1) will not be exact for the pulse-train pre-saturation introduced below, which includes both labeling pulses and inter-pulse delays, but may still provide a reasonable approximation. Based on Equation (1), the APT effect increases with the length of the RF saturation time, which should preferably be approximately or greater than the water  $T_1$  to produce a sufficiently large effect.

In tissue, most proteins and peptides are present in  $\mu\text{M}$  concentrations, and all contain multiple backbone amide protons. The amide proton exchange rate measured using MR spectroscopy was found to be about 30 Hz in the original APT paper and has been assumed widely in APT studies since.<sup>1</sup> However, MR spectroscopy detects mainly the slowly exchanging protons, and the amide proton exchange rate likely has a range of tens to hundreds of Hz in vivo, as reported in later imaging studies.<sup>69–71</sup> These various amide groups resonate at a similar frequency (around 8.3 ppm in the  $^1\text{H}$  spectrum, or with an offset  $\Delta\omega$  of +3.5 ppm downfield from the water resonance).

TABLE 1 Key abbreviations and nomenclature commonly used with APTw imaging

General definitions	
APT	Amide proton transfer
APT <sub>w</sub>	Amide proton transfer-weighted
CEST	Chemical exchange saturation transfer
DS	Direct water saturation
MTC	Magnetization transfer contrast
Pulse sequence parameters	
TR	Repetition time ( $= T_{\text{rec}} + T_{\text{sat}} + T_{\text{acq}}$ )
TE	Echo time
$T_{\text{rec}}$	Magnetization recovery/relaxation delay time before the saturation period
$T_{\text{sat}}$ or $T_{\text{prep}}$	Total RF saturation time or preparation period, which may consist of different combinations of RF pulses and interpulse delays and during which saturation is applied and transfer occurs
$T_{\text{acq}}$	Acquisition time (from excitation through end of acquisition), which may include the lipid suppression time
CW	Continuous wave
$t_p$	Individual pulse element duration in a pulse train or a pulsed steady state
$t_d$	Interpulse delay
$n$	Number of pulse element-delay repetitions
DC <sub>sat</sub>	Saturation duty cycle ( $= t_p / [t_p + t_d]$ )
$B_1$	RF saturation field strength (amplitude)
$B_{1\text{rms}}$ or $B_{1\text{cwpe}}$	Root-mean-square or CW-equivalent power/amplitude of a pulse train
Acquisition terminology	
Z-spectrum	Normalized water saturation signal ( $S_{\text{sat}}/S_0$ ) as a function of frequency offset relative to the water resonance, downfield and upfield
$\Delta\omega$	RF saturation frequency offset relative to the water resonance
Downfield ( $+\Delta\omega$ )	At higher resonance frequency, left side of the spectrum (higher ppm)
Upfield ( $-\Delta\omega$ )	At lower resonance frequency, right side of the spectrum (lower ppm)
$S_{\text{sat}}$ (+3.5 ppm)	APT-label water signal intensity after saturation
$S_{\text{sat}}$ (-3.5 ppm)	Reference water signal intensity after saturation
$S_0$	Control signal intensity without saturation
2-offset or 3-point APTw MRI	Saturation at offsets of $\pm 3.5$ ppm from water and without saturation
6-offset or 7-point APTw MRI	Saturation at offsets of $\pm 3$ , $\pm 3.5$ , and $\pm 4$ ppm from water and without saturation, for example
WASSR	Water saturation shift referencing, used to map $B_0$ inhomogeneity
CEST-Dixon method	An intrinsic $\Delta B_0$ mapping method using echo shifts of 3 $S_{\text{sat}}$ (+3.5 ppm) images
Data processing terms	
MTR	Magnetization transfer ratio ( $= 1 - S_{\text{sat}}/S_0$ )
MTR <sub>asym</sub>	MTR asymmetry relative to the water frequency positioned at 0 ppm
MTR <sub>asym</sub> (3.5 ppm)	MTR asymmetry at 3.5 ppm, used in APTw MRI, equal to APTR + MTR' <sub>asym</sub> (3.5 ppm)
APTR	Amide proton transfer ratio
MTR' <sub>asym</sub> (3.5 ppm)	Exchange-relayed NOE of aliphatic protons of mobile macromolecules and inherent asymmetry of the solid-like MTC effect
rNOE	Exchange-relayed nuclear Overhauser effect
MTC <sub>asym</sub>	Inherent asymmetry of the conventional MTC effect
$k_{\text{sw}}$ or $k_{\text{pa}}$	Solute-proton to water-proton exchange rate
$k_{\text{ws}}$ or $k_{\text{ab}}$	Water-proton to solute-proton exchange rate
$f_s$ or $f_b$	Solute proton population fraction = [solute proton]/[water proton]
$R_{1w}$ or $R_{1a}$	Longitudinal relaxation rate of water = $1/T_{1w}$ or $1/T_{1a}$
$\alpha$	Solute proton saturation efficiency

TABLE 2 Selected APTw imaging technique development papers using  $MTR_{\text{asym}}$  (3.5 ppm) on 3 T clinical MRI systems

No.	Hardware	Pulse sequence			RF saturation parameters	Lipid suppression, readout	Acquisition protocol	Disease	Results	Ref.
		RF saturation approach	RF saturation approach	RF saturation approach						
G1	GE Signa HDxt, Body coil TX	CW		$T_{\text{sat}} = 240 \text{ ms}, B_1 = 0.5/1.5 \mu\text{T}$	Single-slice, Single-shot, spin-echo EPI	Z-spectrum	Brain tumor ( $n = 8$ )	Tumor APTw = $-0.49\%$ ( $0.5 \mu\text{T}$ ) or $0.17\%$ ( $1.5 \mu\text{T}$ )	Scheidegger et al <sup>199</sup>	
G2	GE MR750w	Pulse train		$t_p = 0.232 \text{ ms}, t_d = 0.328 \text{ ms}, n = 6250,$ $DC_{\text{sat}} = 41\%, T_{\text{sat}} = 3.5 \text{ s}, B_1 = 1.75 \mu\text{T}$	Single-slice, single-shot EPI	Z-spectrum	Phantoms		Miyoshi et al. <sup>200</sup>	
G3	GE Discovery MR750	CW		$T_{\text{sat}} = 400 \text{ ms}, B_1 = 2 \mu\text{T}$		Z-spectrum	Brain tumor ( $n = 42$ )	High/low-grade APTw = $3.6\%/2.6\%$	Su et al <sup>31</sup>	
G4	GE Signa	Pulse train		$t_p = 40 \text{ ms}, t_d = 40 \text{ ms}, n = 50,$ $DC_{\text{sat}} = 50\%, T_{\text{sat}} = 4 \text{ s}, B_1 = 1 \mu\text{T}$	Single-slice EPI	Z-spectrum	Stroke ( $n = 55$ )	Good stroke visualization	Lin et al <sup>201</sup>	
G5	GE Discovery MR750	Pulse train		$t_p = 400 \text{ ms}, t_d = 0 \text{ ms}, n = 4,$ $DC_{\text{sat}} = 100\%, T_{\text{sat}} = 1.6 \text{ s}, B_1 = 2 \mu\text{T}$		Z-spectrum	Brain tumor ( $n = 17$ )	Tumor APTw = $2.3\%$	Su et al <sup>198</sup>	
G6	GE Discovery MR750	Pulse train		$t_p = 400 \text{ ms}, t_d = 0 \text{ ms}, n = 3,$ $DC_{\text{sat}} = 100\%, T_{\text{sat}} = 1.2 \text{ s}, B_1 = 1.5 \mu\text{T}$	Single-slice, SE-EPI	Z-spectrum	Brain tumor ( $n = 30$ )	Tumor recurrence APTw = $1.6\%$	Liu et al <sup>45</sup>	
G7	GE Signa Pioneer	Pulse train		$t_p = 500 \text{ ms}, t_d = 0 \text{ ms}, n = 4,$ $DC_{\text{sat}} = 100\%, T_{\text{sat}} = 2 \text{ s}, B_1 = 2 \mu\text{T}$	Single-slice EPI	Z-spectrum	Brain tumor ( $n = 51$ )	Grade-4/3/2 APTw contrast = $4.0\%/2.2\%/1.0\%$	Xu et al <sup>54</sup>	
P1	Philips Intera, Head coil TX/RX	CW		$T_{\text{sat}} = 3 \text{ s}, B_1 = 3 \mu\text{T}$	Single-slice TSE	Z-spectrum	Brain tumor ( $n = 10$ )	APT-hot tumor = $2.7\%$	Jones et al <sup>22</sup>	
P2	Philips Achieva, Body coil TX	CW		$T_{\text{sat}} = 500 \text{ ms}, B_1 = 4 \mu\text{T}$	Single-slice TSE	6-offset	Brain tumor ( $n = 9$ )	High/low-grade APTw = $2.9\%/1.2\%$	Zhou et al <sup>23</sup>	
P3	Philips Achieva, Body coil TX	CW		$T_{\text{sat}} = 500 \text{ ms}, B_1 = 3 \mu\text{T}$	Single-slice TSE	Z-spectrum	Brain tumor ( $n = 12$ )	High-grade APTw = $3.8\%$	Wen et al <sup>24</sup>	
P4	Philips Achieva, Body coil TX	CW		$T_{\text{sat}} = 500 \text{ ms}, B_1 = 1, 2, 3 \mu\text{T}$	Single-slice TSE	Z-spectrum	Brain tumor ( $n = 8$ ), Stroke ( $n = 4$ )	Optimal $B_1 = 2 \mu\text{T}$	Zhao et al <sup>142</sup>	
P5	Philips Achieva, Body coil TX	CW		$T_{\text{sat}} = 500 \text{ ms}, B_1 = 2 \mu\text{T}$	3D TSE	6-offset	Brain tumor ( $n = 8$ )	High-grade APTw = $2.4\%$ (GRE) or $2.3\%$ (WASSR)	Zhao et al <sup>156</sup>	
P6	Philips Achieva, Body coil TX	Pulse train		$t_p = 200 \text{ ms}, t_d = 10 \text{ ms}, n = 4,$ $DC_{\text{sat}} = 95\%, T_{\text{sat}} = 830 \text{ ms}, B_1 = 2 \mu\text{T}$	Frequency-modulated, 3D GRASE	Z-spectrum	Healthy ( $n = 5$ )	White matter APTw = $0.4\%$	Zhu et al <sup>122</sup>	
P7	Philips Achieva, Body coil TX	Time-interleaved pTX		$t_p = 62.5 \text{ ms}, t_d = 0 \text{ ms}, n = 48,$ $DC_{\text{sat}} = 100\%, T_{\text{sat}} = 3 \text{ s}, B_{1\text{rms}} = 1.8 \mu\text{T}$	Single-slice, GRE, TSE	6-offset	Healthy ( $n = 1$ )		Keupp et al <sup>150</sup>	

(Continues)

TABLE 2 (Continued)

No.	Hardware	Pulse sequence		RF saturation parameters	Lipid suppression, readout	Acquisition protocol	Disease	Results	Ref.
		RF saturation approach	RF suppression, readout						
P8	Philips Achieva, Body coil TX	Pulse train	Frequency-modulated, 3D GRASE	$t_p = 200$ ms, $t_d = 10$ ms, $n = 4$ , $DC_{sat} = 95\%$ , $T_{sat} = 830$ ms, $B_1 = 2$ $\mu$ T	6-offset	Brain tumor ( $n = 14$ )	High/low-grade APTw = 2.5%/1.0%	Zhou et al <sup>25</sup>	
P9	Philips Achieva, Body coil TX	Time-interleaved pTX	Single-slice, Single-shot TSE	$t_p = 50$ ms, $t_d = 0$ ms, $n = 40$ , $DC_{sat} = 100\%$ , $T_{sat} = 2$ s, $B_{1rms} = 2$ $\mu$ T	Z-spectrum	Brain tumor ( $n = 36$ )	Grade-4/3/2 APTw = 4.1%/3.2%/2.1%	Togao et al <sup>26</sup>	
P10	Philips Achieva	Pulsed steady-state	3D GRE EPI	$t_p = 70$ ms, $t_d = 70$ ms, $DC_{sat} = 50\%$ , $B_{1peak} = 1$ $\mu$ T	Z-spectrum	Brain tumor ( $n = 45$ )	High/low-grade APTw histogram @90% = 4.1%/2.1%	Park et al <sup>136</sup>	
P11	Philips Ingenia, Body coil TX	Time-interleaved pTX	SPIR, 3D TSE, CS-SENSE factor = 4	$t_p = 50$ ms, $t_d = 0$ ms, $n = 40$ , $DC_{sat} = 100\%$ , $T_{sat} = 2$ s, $B_{1rms} = 2$ $\mu$ T	6-offset	Brain tumor ( $n = 6$ )	High-grade APTw = 3.5%	Heo et al <sup>164</sup>	
S1	Siemens Magnetom TIM Trio	Pulse train	Single-slice, Single-shot EPI	$t_p = 20$ ms, $t_d = 20$ ms, $n = 75$ , $DC_{sat} = 50\%$ , $T_{sat} = 3$ s, $B_1 = 0.6$ $\mu$ T	Z-spectrum	Healthy ( $n = 4$ )	White matter APTw = -4.2%	Sun et al <sup>125</sup>	
S2	Siemens Magnetom, Knee coil TX/RX	Pulse train	Single-slice, Single-shot EPI	$t_p = 100$ ms, $t_d = 100$ ms, $n = 10$ , $DC_{sat} = 50\%$ , $T_{sat} = 2$ s, $B_{1rms} = 2$ $\mu$ T	Z-spectrum	Phantoms		Schmitt et al <sup>126</sup>	
S3	Siemens Magnetom Trio	Pulse train	3D GRE	$t_p = 100$ ms, $t_d = 100$ ms, $n = 3$ , $DC_{sat} = 50\%$ , $T_{sat} = 600$ ms, $B_{1rms} = 2$ $\mu$ T	Z-spectrum	Brain tumor ( $n = 26$ )	High/low-grade APTw = 1.3%/0.8%	Sakata et al <sup>27</sup>	
S4	Siemens Skyra	Pulsed steady-state	TurboFLASH	$t_p = 20-90$ ms, $DC_{sat} = 45-80\%$ , $B_{1rms} = 0.76-1.5$ $\mu$ T	Z-spectrum	Phantoms		Yoshimaru et al <sup>137</sup>	
S5	Siemens Magnetom Trio	Pulse train	Single-slice, GRE	$t_p = 99$ ms, $t_d = 100$ ms, $n = 5$ , $DC_{sat} = 50\%$ , $T_{sat} = 895$ ms, $B_{1rms} = 2$ $\mu$ T	Z-spectrum	Brain tumor ( $n = 44$ )	Grade-4/3/2 APTw = 2.1%/1.7%/1.3%	Bai et al <sup>132</sup>	
S6	Siemens Prisma, Body coil TX	Pulse train	SPIR, 3D TSE, SPACE	$t_p = 100$ ms, $t_d = 10$ ms, $n = 10$ , $DC_{sat} = 91\%$ , $T_{sat} = 1.1$ s, $B_{1rms} = 2.38$ $\mu$ T	6-offset	Brain tumor ( $n = 3$ )	High-grade APTw = 3.3% (TSE) or 3.2% (SPACE)	Zhang et al <sup>149</sup>	
S7	Siemens Prisma, Body coil TX	Pulse train	3D snapshot-GRE	$t_p = 50$ ms, $t_d = 5$ ms, $n = 36$ , $DC_{sat} = 91\%$ , $T_{sat} = 2$ s, $B_{1rms} = 2$ $\mu$ T	Z-spectrum	Brain tumor ( $n = 1$ )	High-grade APTw hyperintensity	Herz et al <sup>129</sup>	
T1	Toshiba Vantage Titan	Pulse train	2D fast advanced spin-echo	$t_p = 40$ ms, $n = 10$ , $B_{1rms} = 1-2$ $\mu$ T	Z-spectrum	Thoracic tumor ( $n = 21$ )	Malignant/benign APTw = 3.6%/0.3%	Ohno et al <sup>128</sup>	

Abbreviations: CS-SENSE, compressed sensing-SENSE; EPI, echo planar imaging; FLASH, fast low angle shot; GRASE, gradient and spin-echo acquisition; GRE, gradient echo; SPACE (optimized TSE), sampling perfection with application optimized contrasts by using different flip angle evolutions; SPIR, spectral presaturation with inversion recovery; TSE, turbo spin echo; TX, transmit; pTX, parallel transmit; RX, receive.

TABLE 3 Selected APT imaging technique development papers using metrics other than  $MTR_{\text{asym}}$  (3.5 ppm) on 3 T clinical MRI systems

Pulse sequence		Lipid suppression, RF saturation		Acquisition protocol		Data processing method, metrics		Disease		Results		Ref.	
No.	Hardware	RF approach	RF saturation parameters	RF saturation readout	Acquisition protocol	Acquisition protocol	Acquisition protocol	Acquisition protocol	Disease	Results	Results	Ref.	Ref.
1	GE Signa Excite, Body coil TX	Pulse train	$t_p = 9$ ms, $t_d = 15$ ms, $n = 200$ , $DC_{\text{sat}} = 60\%$ , $T_{\text{sat}} = 3$ s, $B_1 = 0.78 \mu\text{T}$	Single-slice, single-shot, spin-echo EPI	SAFARI, $S_{\text{sat}}(\Delta\omega)$ , $S_{\text{sat}}(\Delta\omega, -\Delta\omega)$ , $S_{\text{sat}}(-\Delta\omega)$ , $S_{\text{sat}}(-\Delta\omega, \Delta\omega)$ , $S_0$	SAFARI, $S_{\text{sat}}(\Delta\omega)$ , $S_{\text{sat}}(\Delta\omega, -\Delta\omega)$ , $S_{\text{sat}}(-\Delta\omega)$ , $S_{\text{sat}}(-\Delta\omega, \Delta\omega)$ , $S_0$	$MTR_{\text{SAFARI}}$ (3.5 ppm)	Healthy ( $n = 4$ )	Healthy ( $n = 4$ )	Normal tissue $MTR_{\text{SAFARI}} = 2.3\%$	Normal tissue $MTR_{\text{SAFARI}} = 2.3\%$	Scheidegger et al <sup>121</sup>	Scheidegger et al <sup>121</sup>
2	GE Discovery MR750	CW	$T_{\text{sat}} = 400$ ms, $B_1 = 2 \mu\text{T}$		Z-spectrum	Z-spectrum	Multi-pool Lorentzian fitting, fitted APT, $MTR_{\text{asym}}$ (3.5 ppm)	Brain tumor ( $n = 32$ )	Brain tumor ( $n = 32$ )	High/low-grade APT = 7.6%/6.8%, APT <sub>w</sub> = 4.3%/4.1%	High/low-grade APT = 7.6%/6.8%, APT <sub>w</sub> = 4.3%/4.1%	Zhang et al <sup>34</sup>	Zhang et al <sup>34</sup>
3	Philips Achieva, Body coil TX	Pulse train	$t_p = 200$ ms, $t_d = 10$ ms, $n = 4$ , $DC_{\text{sat}} = 95\%$ , $T_{\text{sat}} = 830$ ms, $B_1 = 2 \mu\text{T}$	Single-slice TSE	Z-spectrum	Z-spectrum	EMR, $MTR_{\text{asym}}$ (3.5 ppm), APT <sup>#</sup> , NOE <sup>#</sup>	Brain tumor ( $n = 11$ )	Brain tumor ( $n = 11$ )	High-grade APT <sub>w</sub> = 3%, APT <sup>#</sup> = 4.5%, NOE <sup>#</sup> = 1.5%	High-grade APT <sub>w</sub> = 3%, APT <sup>#</sup> = 4.5%, NOE <sup>#</sup> = 1.5%	Heo et al <sup>96</sup>	Heo et al <sup>96</sup>
4	Philips Achieva, Body coil TX	Pulse train	$t_p = 242.5$ ms, $t_d = 2.5$ ms, $n = 4$ , $DC_{\text{sat}} = 95\%$ , $T_{\text{sat}} = 977.5$ ms, $B_{1\text{rms}} = 0.52 \mu\text{T}$	SPIR, Single-slice, Single-shot fast field echo EPI	Z-spectrum	Z-spectrum	Multi-pool Lorentzian fitting, $AUC_{\text{amide}}$ , $MTR_{\text{amide}}$ , $MTR_{\text{asym}}$ (3.5 ppm)	Brain tumor ( $n = 16$ )	Brain tumor ( $n = 16$ )	Tumor progression $AUC_{\text{amide}} = 3\%$ Hz, $MTR_{\text{amide}} = 12\%$ , APT <sub>w</sub> = -0.6%	Tumor progression $AUC_{\text{amide}} = 3\%$ Hz, $MTR_{\text{amide}} = 12\%$ , APT <sub>w</sub> = -0.6%	Mehrabian et al <sup>202</sup>	Mehrabian et al <sup>202</sup>
5	Philips Achieva, Body coil TX	Pulse train	$t_p = 16.8$ , $33.6$ ms, $t_d = 39.2$ , $78.4$ ms, $DC_{\text{sat}} = 30\%$ , $T_{\text{sat}} = 2$ s, $B_{1\text{rms}} = 0.5 \mu\text{T}$	Single-slice, single-shot spin-echo EPI	CERT, $S_x(\Delta\omega)$ , $S_{2x}(\Delta\omega)$ , $S_0$	CERT, $S_x(\Delta\omega)$ , $S_{2x}(\Delta\omega)$ , $S_0$	$MTR_{\text{double}}$	Healthy ( $n = 6$ )	Healthy ( $n = 6$ )	White matter APT = 1.5%, rNOE = 2.1%	White matter APT = 1.5%, rNOE = 2.1%	Lin et al <sup>138</sup>	Lin et al <sup>138</sup>
6	Siemens Verio	Pulse train	$t_p = 20$ ms, $t_d = 20$ ms, $n = 50$ , $DC_{\text{sat}} = 50\%$ , $T_{\text{sat}} = 2$ s, $B_{1\text{rms}} = 0.55 \mu\text{T}$	Single-slice, Spin-echo EPI	Z-spectrum	Z-spectrum	3-pool BM equation analysis, $MTR_{\text{asym}}$ (3.5 ppm)	Stroke ( $n = 6$ )	Stroke ( $n = 6$ )	Good stroke detection	Good stroke detection	Tee et al <sup>127</sup>	Tee et al <sup>127</sup>
7	Siemens Magnetom Prisma, Body coil TX	Pulse train	$t_p = 20$ ms, $t_d = 20$ ms, $n = 80$ , $DC_{\text{sat}} = 50\%$ , $T_{\text{sat}} = 3.2$ s, $B_{1\text{mean}} = 0.6 \mu\text{T}$	3D snapshot-GRE	Z-spectrum	Z-spectrum	Multi-pool Lorentzian fitting, $A_{+3.5\text{ppm}}$	Healthy ( $n = 3$ ), Brain tumor ( $n = 1$ )	Healthy ( $n = 3$ ), Brain tumor ( $n = 1$ )	Tumor $A_{+3.5\text{ppm}} = 4.2\%$	Tumor $A_{+3.5\text{ppm}} = 4.2\%$	Deshmane et al <sup>158</sup>	Deshmane et al <sup>158</sup>
8	Siemens Magnetom Prisma, Body coil TX	Pulse train	$t_p = 20$ ms, $t_d = 5$ ms, $n = 148$ , $DC_{\text{sat}} = 80\%$ , $T_{\text{sat}} = 3.7$ s, $B_{1\text{mean}} = 0.6, 0.9 \mu\text{T}$	3D snapshot-GRE	Z-spectrum	Z-spectrum	Multi-pool Lorentzian fitting, $MTR_{\text{REX}}$ , AREX	Healthy ( $n = 1$ ), Brain tumor ( $n = 1$ )	Healthy ( $n = 1$ ), Brain tumor ( $n = 1$ )	Decreased tumor $MTR_{\text{REX}}$ and AREX	Decreased tumor $MTR_{\text{REX}}$ and AREX	Goerke et al <sup>203</sup>	Goerke et al <sup>203</sup>
9	Siemens Magnetom Prisma	Pulse train	$t_p = 100$ ms, $t_d = 61$ ms, $n = 5$ , $DC_{\text{sat}} = 62\%$ , $T_{\text{sat}} = 744$ ms, $B_1 = 2 \mu\text{T}$	3D GRE	Z-spectrum	Z-spectrum	Integral $MTR_{\text{asym}}$ ( $3.5 \pm 0.4$ ppm)	Brain tumor ( $n = 26$ )	Brain tumor ( $n = 26$ )	High/low-grade APT <sub>w</sub> = 2.6%/1.5%	High/low-grade APT <sub>w</sub> = 2.6%/1.5%	Durmo et al <sup>137</sup>	Durmo et al <sup>137</sup>

Abbreviations: #, EMR-based CEST metrics; AREX, apparent exchange-dependent relaxation; AUC, area under the curve; BM, Bloch-McConnell; CERT, chemical exchange rotation transfer; EMR, extrapolated semisolid magnetization transfer reference; EPI, echo planar imaging; GRE, gradient echo;  $MTR_{\text{double}}$ , subtraction of signals using  $\pi$  from  $2\pi$  pulses;  $MTR_{\text{REX}}$ , subtraction of inverse Z-spectra; SAFARI, saturation with frequency alternating RF irradiation; SPIR, spectral presaturation with inversion recovery; TSE, turbo spin echo; TX, transmit; pTX, parallel transmit; RX, receive.

This leads to a large composite resonance in NMR spectroscopy that reflects a total accessible amide proton concentration of approximately 50-100 mM (hence, justifying the assumption that  $f_s k_{sw} < R_{1w}$  in Equation [1]).<sup>1,69-71</sup> The magnitude of the APTR effect in vivo resulting from these protons is typically on the order of a few percent of the bulk water signal. Although this is a small effect on the water signal, APTw MRI offers a large detection sensitivity enhancement for metabolites present in millimolar concentrations.

The sum of all saturation effects at a certain offset ( $\Delta\omega$ ) is generally described in terms of the magnetization transfer ratio (MTR):

$$MTR(\Delta\omega) = 1 - Z(\Delta\omega) = 1 - S_{\text{sat}}(\Delta\omega)/S_0, \quad (2)$$

where  $S_{\text{sat}}$  and  $S_0$  are, respectively, water signal intensities with and without RF saturation,  $\Delta\omega$  is the irradiation frequency offset using the water frequency as a 0-frequency reference, and  $Z = S_{\text{sat}}/S_0$  is the signal intensity in the water saturation spectrum ( $Z$ -spectrum). When performing an APTw experiment in vivo, DS and conventional semi-solid magnetization transfer contrast (MTC)<sup>72</sup> effects will interfere with the measurement (Figure 1). APTw imaging is usually quantified in terms of an MTR asymmetry ( $MTR_{\text{asym}}$ ) analysis with respect to the water frequency (0 ppm in the  $Z$ -spectrum) at an offset of  $\pm 3.5$  ppm<sup>12</sup>:

$$\begin{aligned} MTR_{\text{asym}}(3.5\text{ppm}) &= MTR(+3.5\text{ppm}) - MTR(-3.5\text{ppm}) \\ &= Z(-3.5\text{ppm}) - Z(+3.5\text{ppm}) \\ &= \frac{S_{\text{sat}}(-3.5\text{ppm}) - S_{\text{sat}}(+3.5\text{ppm})}{S_0} \\ &= APTR + MTR'_{\text{asym}}(3.5\text{ppm}), \quad (3) \end{aligned}$$

where  $MTR'_{\text{asym}}(3.5\text{ppm})$  includes the exchange-relayed nuclear Overhauser effect (rNOE) of aliphatic protons in mobile macromolecules<sup>6,73-75</sup> and the inherent asymmetry of the conventional semi-solid MTC effect ( $MTC_{\text{asym}}$ ).<sup>76</sup> These and a few other possible contributions are discussed in the next section. The rNOE in the upfield  $Z$ -spectrum originates from the intramolecular magnetic interaction between aliphatic and exchangeable protons of mobile macromolecules, which relays the saturation effect to the water signal via subsequent exchange. Like APTR, the rNOE and  $MTC_{\text{asym}}$  contribute in an amount that depends on the RF parameters used.<sup>77</sup> Because of the presence of other contributions,  $MTR_{\text{asym}}(3.5\text{ppm})$  images are often called APTw images.<sup>23</sup>

### 3 | HISTORY OF THE MECHANISM AND THE EVOLUTION OF ITS UNDERSTANDING

Originally, APTw imaging was designed for in vivo imaging of mobile protein content in tumors and pH changes in tissue during ischemia (because of the strong dependence of the amide proton exchange rate on pH in the physiological range).<sup>1,2</sup> It exploits the concept that the CEST mechanism can detect changes in amide proton signals. These 2 applications are based on early spectroscopy studies that showed an increased amide proton signal in proton spectra during ischemia (because of slower exchange)<sup>78</sup> and very large amide proton signals in perfused tumor cells.<sup>78,79</sup> These hypotheses were confirmed in vivo where ischemia experiments in rats at 4.7 T showed a small decrease in  $MTR_{\text{asym}}$  spectra over a chemical shift range of 2.5 to 5 ppm from the water, with the clearest decrease at 3.5 ppm, attributed to reduced pH.<sup>1</sup> The first in vivo studies in animal tumor models at the same field and RF settings showed a broad, increased  $MTR_{\text{asym}}$  effect ranging from 1.5 to 5 ppm.<sup>2</sup> In that paper, the signal change over this range was attributed to backbone amide and other exchangeable protons, which are typically seen in this range in high-resolution NMR protein studies and in the MR spectra of perfused cells and brain. Because of the results of MR spectroscopy, the authors focused on the 3.5 ppm offset.

In early work,<sup>2</sup> the increased APTw signal in tumors (relative to normal brain tissue) was attributed to (1) the increased mobile amide proton concentration in the tumor associated with the increased concentration of mobile cytosolic proteins and peptides because of higher cellularity, and (2) the slightly increased amide proton exchange rate because of marginally higher intracellular pH (<0.1 unit, as reported from phosphorus MR spectroscopy studies in patients)<sup>80-82</sup> in tumor cells. This has been confirmed in subsequent studies<sup>83-86</sup> and is consistent with increasing protein concentrations in tumors, as revealed by proteomics<sup>87,88</sup> and by in vivo MR spectroscopy.<sup>89</sup> It has been reported that solid tumors have an acidic extracellular pH and a neutral-to-alkaline intracellular pH.<sup>90,91</sup> Notably, reduced acidic extracellular pH in tumors would substantially reduce the amide exchange rate and, therefore, the contribution of extracellular proteins and peptides. The intracellular origin is supported by a recent study showing that there was no correlation between the amide proton exchange rate and extracellular pH.<sup>92</sup>

Over the years, the understanding of the APTw contrast mechanism has evolved. Several other possible effects that may contribute to the APTw hyperintensity in tumors include: (3) reduced semi-solid  $MTC_{\text{asym}}$  (3.5 ppm) in tumors because their  $Z$ -spectra are less asymmetric than in white matter and gray matter. This effect



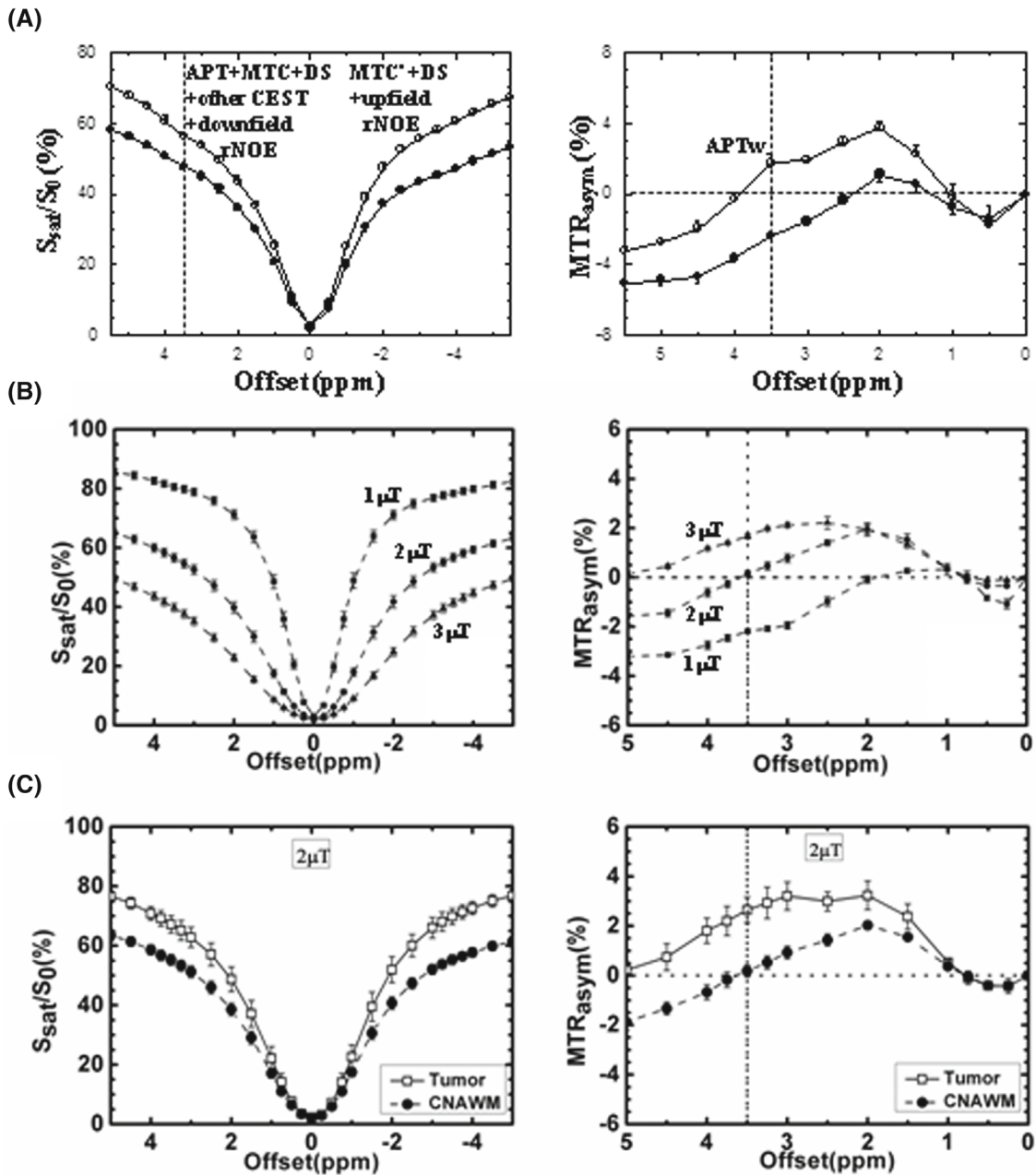


**FIGURE 1** (A) Z-spectra and MTR<sub>asymp</sub> spectra measured from a 9L rat brain tumor model at 4.7 T (12 days post-implantation,  $n = 6$ ,  $T_{sat} = 4$  s,  $B_1 = 1.3$  μT). Tumor: open circles; contralateral normal brain tissue: solid circles. The APT effect is visible as a small resonance at the offset of 3.5 ppm in the Z-spectrum. The effect is stronger in the tumor than in the contralateral normal region. There is a small difference between the downfield and upfield semi-solid MTC effects (namely, MTC vs. MTC') in normal tissue, which is reduced in the tumor. Reproduced with permission and with some additions from Salhotra et al.<sup>197</sup> (B) Z-spectra and MTR<sub>asymp</sub> spectra of white matter from healthy subjects ( $n = 4$ ), obtained at 3 T with 3 different RF saturation strengths and  $T_{sat} = 500$  ms. The error bars are too small to see clearly. White matter MTR<sub>asymp</sub>(3.5 ppm) is roughly 0 at 2 μT. (C) Z-spectra and MTR<sub>asymp</sub> spectra measured from brain tumor patients at 3 T ( $n = 8$ ,  $T_{sat} = 500$  ms,  $B_1 = 2$  μT). Tumor: open squares; contralateral normal-appearing white matter (CNAWM): solid circles. The APT<sub>w</sub> signal is stronger in the tumor than in the CNAWM. (B) and (C) reproduced with permission from Zhao et al.<sup>142</sup>

becomes more visible when using a longer saturation time, with  $B_1$  increasing from 0.5 to 3 μT.<sup>76,93</sup> (4) Decreased aliphatic rNOEs of mobile macromolecules at and around the opposite frequency offset -3.5 ppm.<sup>6,73-75</sup> Based on Equation (3), the MTR<sub>asymp</sub>-based APT<sub>w</sub> image signal

has multiple contributions (primarily including aliphatic rNOE and MTC<sub>asymp</sub>). In the brain, MTR<sub>asymp</sub>(3.5 ppm) ( $\approx -rNOE - MTC_{asymp}$ ) is negative and reduces the MTR<sub>asymp</sub> (3.5 ppm). Therefore, this contribution is actually a synergistic factor that enhances the APT<sub>w</sub> image

contrast of the tumor because of the reductions in aliphatic rNOE and  $MTC_{\text{asym}}$  in tumors relative to brain tissue.<sup>94–96</sup> (5) Downfield rNOEs (e.g., in aromatic residues). This possible confounder at and around +3.5 ppm downfield of water has been previously explored in studies of protein solutions, tissue homogenates, and brains in vivo, and will partially counteract the aliphatic rNOE contribution.<sup>97,98</sup> (6) Spillover and MTC dilution effects.<sup>67</sup> When performing the  $MTR_{\text{asym}}$  analysis, asymmetric effects relative to water are visualized, and symmetric background signals (water  $T_2$  [ $T_{2w}$ ]-based spillover and the symmetric portion of MTC) are removed under the zeroth-order approximation. However, the APT effect is always diluted by competing spillover and MTC effects, resulting in the fact that  $T_{2w}$  and MTC alterations may influence the magnitude of APTw contrast. (7) Contamination by  $T_{1w}$  changes<sup>67</sup> (but there is a nonlinear relationship between APTw and  $T_{1w}$ ). As shown in Equation (1), the APT effect scales with  $T_{1w}$ . However, the effects of increased  $T_{1w}$  (decreased  $R_{1w}$ ) and water content (denominator of  $f_s$ ) in brain tumors are canceled out partially.<sup>84</sup> Further, apart from the  $T_{1w}$  recovery effect, there is an opposing  $T_{1w}$  effect on APTw through dilution effects, as longer  $T_{1w}$  leads to lower  $Z$ -spectra, therefore, increasing the dilution effects, which lowers the APT effect.<sup>99</sup> These 2 effects cancel each other out to some extent, depending on experimental RF settings. Simulation studies have shown that APTw increases with  $T_{1w}$  at lower  $B_1$ , but is roughly insensitive to  $T_{1w}$  or even decreases with  $T_{1w}$  at higher  $B_1$ .<sup>99,100</sup> In addition, the dependence of APTw MRI on  $T_{1w}$  can be reduced using non-steady-state saturation. Fortunately, when RF strength is approximately equal to 2  $\mu$ T (as recommended for brain tumor imaging at 3 T), APTw intensity has been found to be reasonably robust against the change in  $T_{1w}$ .<sup>99,100</sup> Therefore, a correction for  $T_{1w}$  changes is not necessary for APTw imaging of brain tumors at 2  $\mu$ T on clinical 3 T scanners. Of course, this robustness still has limits.<sup>101,102</sup> Because the significant  $T_{1w}$  effect of Gd contrast agents may bias APTw imaging, it is important to remember that the APTw acquisition should always be performed before the injection of contrast agents.<sup>103</sup> (8) CEST signals from exchangeable protons resonating nearby. At 3 T, most exchangeable protons (of macromolecules and metabolites (such as amines and hydroxyls) are in the fast-exchange regime ( $k_{sw} \gg \Delta\omega_s$ ), and their resonances start to coalesce with water. Reduced extracellular pH in tumors may reduce the exchange rates of extracellular amines and other fast-exchanging protons and make them become detectable.<sup>104</sup> It is worth noting that the linewidth of some nearby intermediate-exchange resonances (including those from guanidinium protons at 2 ppm, which have an exchange rate of about 800-1000 Hz<sup>105,106</sup> and, therefore, an effective linewidth of about 2.0-2.5 ppm at 3 T)

may be sufficiently large to be partially irradiated and detected at 3.5 ppm.<sup>107,108</sup> (9) APTw effect from mobile proteins in liquefactive necrosis. Proteinaceous fluid compartments in tumors, such as liquefactive necrosis, would result in large hyperintensity on APTw images<sup>12,24</sup> because of the abundance of proteins and protein fractions at higher mobility. In addition, plausible protein denaturation processes would generate such a signal increase.<sup>109,110</sup> Notably, reduced dilution effects in liquefactive necrosis would lead to an apparently high APTw contrast between this compartment and normal brain tissue. To simplify radiology readings, a new APTw metric based on the background MTR value has been proposed to suppress APTw signals of large liquefactive necrosis.<sup>111</sup> However, a further validation is needed for this APTw metric. (10) APTw effect from mobile proteins in blood vessels and hemorrhage. Blood has high concentrations of hemoglobin in erythrocytes and albumin in plasma, and a higher pH ( $\sim 0.2$  pH units, relative to brain tissue),<sup>112</sup> which would contribute to the increased APTw in well-perfused tumors because of induced angiogenesis.<sup>37,113</sup> In addition, like liquefactive necrosis, intratumoral hemorrhage would demonstrate large APTw hyperintensity, particularly at hyperacute and acute stages.<sup>24,114,115</sup>

Given all these potential synergistic or competitive effects, the contributions of which are affected by experimental RF settings and analysis approaches, the question arises whether the chosen term “APT-weighted” imaging is still justified, because it implies that the APT component is the major source of this signal. With the above list as a reference and amide protons as one important contributor, this naming is valid under the careful choice of acquisition and analysis.<sup>94–96</sup> For clinical APTw imaging of brain tumors, we would seek a pragmatic compromise that not only effectively detects APT, but also can be standardized so that all other effects are consistent between vendors and studies. Notably, recent radiographic-histopathologic correlation studies<sup>26,29,43</sup> have clearly demonstrated that  $MTR_{\text{asym}}$ (3.5 ppm) is a valid metric that adds clinical value to the imaging of brain tumors at 3 T. Further validation is still needed on different pathology types for the various recommended APTw approaches described below.

In light of the above list of possible confounding contributions, there is still a great need for continued work on CEST methods with increased signal specificity and/or parameter quantification, as such methods may ultimately have improved diagnostic use. Some of such pulse sequences and data analyses that attempt to separate APT effects from the other contributions in APTw imaging are discussed in Table 3 and “Data Processing” below. Additional methods that incorporate different (and sometimes radically different) acquisition protocols are

reviewed elsewhere.<sup>116,117</sup> The current paper is focused solely on providing a reasonable standard for assessing brain tumors in daily clinical practice using a currently established  $MTR_{\text{asym}}$ -based APTw approach.

## 4 | PULSE SEQUENCES

### 4.1 | RF saturation approaches and parameters

Currently, no consensus-based APTw MRI pulse sequences or parameters are available for clinical MRI systems between different vendors, even for the most studied application of brain tumors. As mentioned above, the APTw signal depends on the APTw pulse sequence features and parameters used. Notably, the APTw signal is affected by dilution effects, the contributions of which vary with the saturation amplitude and time. Because of this dependence, to achieve reproducible APTw imaging contrast for brain tumors, a consensus choice of certain saturation parameters is needed. Based on the abundant literature of the last decade, and taking into account saturation time limitations for amplifiers on some equipment, we recommend:

$$\begin{aligned} APTw = MTR_{\text{asym}} (3.5\text{ppm}, B_{1\text{rms}} = 2 \mu\text{T}, \\ T_{\text{sat}} > 0.8 \text{ s}, DC_{\text{sat}} \geq 50\%), \end{aligned} \quad (4)$$

where  $T_{\text{sat}}$  (during which saturation is applied and transfer occurs) may consist of different combinations of RF pulses and inter-pulse delays,  $DC_{\text{sat}}$  is the RF saturation duty cycle (DC), and  $B_{1\text{rms}}$  is the root-mean-square  $B_1$  value of a saturation pulse train with duration  $t_p$  and inter-pulse delay  $t_d$ , defined as:

$$B_{1\text{rms}} = \sqrt{\frac{1}{t_p + t_d} \int_0^{t_p} [B_1(t)]^2 dt}. \quad (5)$$

Notably, Equation (4) provides some flexibility that is needed at this stage. However, to enhance reproducibility and the comparison of results across vendors and sites, our preferred and more specific recommendation as a long-term goal is:

$$\begin{aligned} APTw = MTR_{\text{asym}} (3.5\text{ppm}, B_{1\text{rms}} = 2 \mu\text{T}, \\ T_{\text{sat}} = 2 \text{ s}, DC_{\text{sat}} \geq 90\%). \end{aligned} \quad (6)$$

The choice of these RF saturation parameters is based on the following rationales.

It has been shown that the APTw contrast in brain tumors ( $T_{1w} \approx 1.5\text{-}1.6 \text{ s}$  in the solid portion of gliomas

at 3 T)<sup>118,119</sup> improves substantially (Figure 2A) when lengthening  $T_{\text{sat}}$  from 0.5 s to 2 s.<sup>120</sup> For clinical APTw imaging, a CW block pulse of several seconds is possible for RF saturation with transmit-receive head coils on a standard 3 T clinical system,<sup>22</sup> similar to typical animal APTw experiments. However, most standard 3 T clinical systems use body coils for transmit, which results in stricter limitations on RF amplifier DC (typically 50%), saturation pulse length, and, to some extent, SAR. In the past decade, this has been addressed by a few different methods (Tables 2 and 3), such as pulse-train, time-interleaved parallel RF transmission (pTX), or pulsed steady state APTw MRI. The pulse-train pre-saturation (a train of pulses separated by brief delays) has been used in some early pre-clinical APTw studies<sup>1,2</sup> and in most 3 T clinical investigations.<sup>121-128</sup> The use of pulse trains can achieve a  $DC_{\text{sat}} > 90\%$  and a  $T_{\text{sat}} > 0.8 \text{ s}$  on most 3 T MRI scanners from different vendors, greatly alleviating the limitations in amplifier duty-cycles and saturation pulse lengths. Notably, in a recent study on a brain tumor patient using different pulse-train RF saturation modules, Herz et al<sup>129</sup> confirmed the decreased tumor APTw signal intensities with decreasing  $DC_{\text{sat}}$  (Figure 2B). To truly maximize the saturation efficiency, Keupp et al<sup>130,131</sup> introduced a time-multiplexed RF saturation method in pTX systems (Figure 3). By time-interleaving 2 RF sources of the body coil (the quadrature channels), each with a 50% idle-time, one can achieve an increased length of the pseudo-CW saturation pulse train, completely meeting the needs of CEST/APTw imaging. Finally, the pulsed steady-state CEST sequence, previously implemented on 1.5T<sup>132</sup> and 7T<sup>128,129</sup> human MRI systems,<sup>133,134</sup> but similar to the 3 T MTC steady-state sequence,<sup>135</sup> is currently being optimized for APTw MRI on 3 T clinical systems.<sup>136-141</sup> With this, the CEST effect is built up over multiple saturation pulses and each is followed by an imaging acquisition segment. However, the DC for such a pulsed steady-state sequence is inherently low.

The amide proton pool, which has a  $k_{\text{sw}}$  range of tens to hundreds of Hz in vivo, can be efficiently labeled using an RF saturation strength ( $B_1$  or  $B_{1\text{rms}}$ ) between 1 and 3  $\mu\text{T}$  (1  $\mu\text{T} = 42.567 \text{ Hz}$ ). Importantly, the use of 2  $\mu\text{T}$  in  $MTR_{\text{asym}}$ -based APTw imaging of brain tumors provides some advantages. When a  $B_1$  of 2  $\mu\text{T}$  is used, the APTw signal is almost 0 for normal brain tissue (Figure 4A), because of the presence of a negative  $MTR'_{\text{asym}}$  (3.5 ppm) compensating the APTR. In addition, the APTw signal should always be negligible in the cerebrospinal fluid (CSF) because of the symmetry of the CSF Z-spectrum. Therefore, using this  $B_1$  and sufficient  $T_{\text{sat}}$  (0.8-2 s), the APTw images are zeroed in most normal brain areas, the ventricles and, in patients, the resection cavity (Figure 4B). This convenient background allows easy detection of

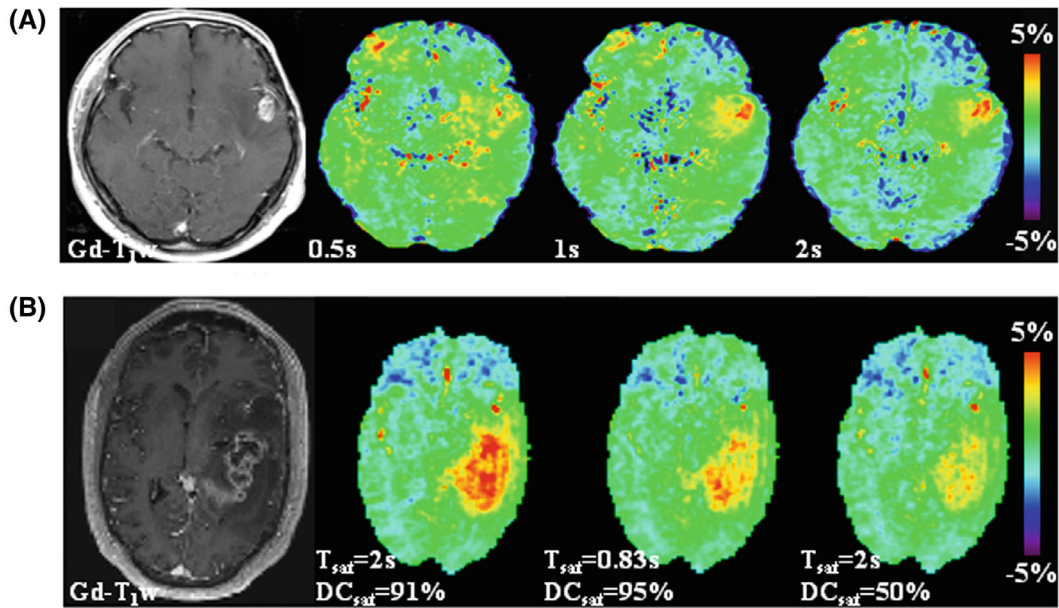
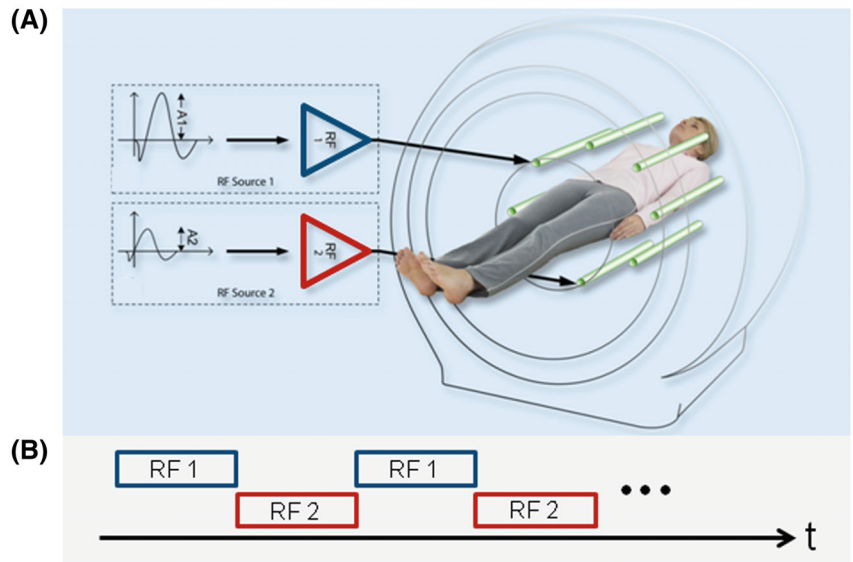


**FIGURE 2** Illustration of the need for a saturation period ( $T_{sat}$ ) on the order of 1-2 s and for a high RF saturation duty cycle ( $DC_{sat}$ ) for APTw MRI of brain tumors at 3 T. Gd-enhanced  $T_1w$  images are included with each example as a morphological reference. (A) An example of APTw MRI ( $B_{1rms} = 2 \mu T$ ,  $DC_{sat} = 100\%$ ) for a patient with glioblastoma showing that the APTw signal in the relevant regions increases with  $T_{sat}$ . Reproduced from Togao et al.<sup>120</sup> (B) APTw and Gd-enhanced  $T_1w$  images for a glioblastoma patient acquired with 3 different pulse-train RF saturation modules ( $B_{1rms} = 2 \mu T$ ). The APTw hyperintensity can be seen clearly in the tumor region relative to normal-appearing brain tissue, the highest for the module ( $T_{sat} = 2 s$ ,  $DC_{sat} = 91\%$ ) and the lowest for the module ( $T_{sat} = 2 s$ ,  $DC_{sat} = 50\%$ ). Reproduced from Herz et al.<sup>129</sup>

**FIGURE 3** Schematic representation of parallel RF transmission (pTX, dual transmit here) (A), alternated over time (B), used for APTw MRI RF saturation. To achieve 100% duty-cycle RF saturation, 2 independent sources, RF1 and RF2, are driven by the RF amplifiers in a time-interleaved fashion, therefore, running each amplifier at 50% duty-cycle and limited pulse duration according to the hardware specifications. Reproduced with permission from Keupp et al.<sup>61,130</sup>



hyperintense APTw signals in high-grade tumors or hypointense APTw signals in ischemic tissue, which is convenient for clinical assessment.<sup>142</sup>

Four RF saturation types (types [a]-[d]) recommended for brain tumor APTw imaging on 3 T clinical MRI scanners are given in Table 4, in which types (a) and (b) are the 2 preferred options. For all pulse-train saturation types, we recommend  $B_{1rms} = 2 \mu T$ ,  $T_{sat} = 0.8-2 s$ ,

and  $DC_{sat} \geq 50\%$ . This recommendation retains some flexibility for the parameters of shaped pulses (such as shape, length, and phase). Type (a) and several examples using type (b) are further compared in Figure 5A and B1-B3. Type (a) is the ideal approach and is allowed only with transmit-receive head coils, some state-of-the-art RF amplifiers, or single-slice APTw imaging protocols. Fortunately, the pulse-train methods in type (b) can be

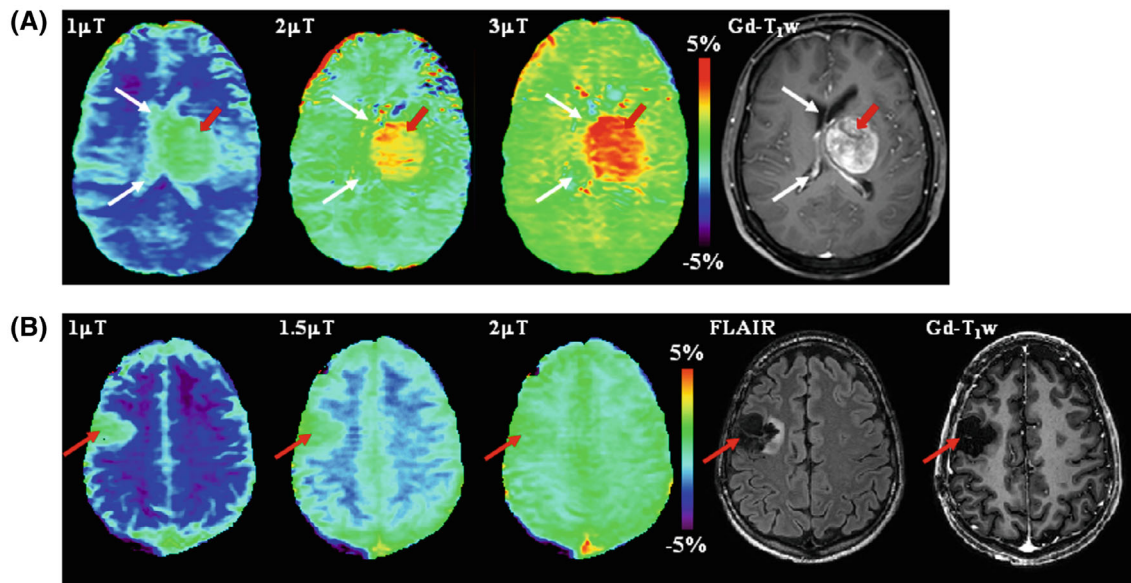


**FIGURE 4** APTw images at 3 T acquired at different RF saturation strengths. (A) A patient with cerebral metastasis. The tumor (red arrows) shows hyperintense signal on all APTw images. However, the lesion margins are poorly delineated on the APTw image at 1  $\mu$ T because of the presence of cerebrospinal fluid (CSF) artifacts (white arrows). Reproduced with permission from Zhao et al.<sup>142</sup> (B) A glioma patient post-treatment. The APTw signals at different  $B_1$  strengths are all around 0 in the resection cavity (as in CSF), but very different in normal brain tissue (Figure 1B). Therefore, at 1  $\mu$ T, the resection cavity (red arrow) shows unexpected apparent APTw hyperintensity. However, the APTw image at 2  $\mu$ T is homogenous for most brain regions, including the resection cavity (red arrow). Notice the residual hyperintensity in the sagittal sinus likely because of the high protein content of blood. Unpublished data from Dr. Hye-Young Heo. The study was approved by the local Institutional Review Board

**TABLE 4** Recommendations for APTw imaging of brain tumors at 3 T

#### Pulse sequences

RF saturation approaches and parameters:

- a CW RF saturation,  $T_{\text{sat}} = 2$  s,  $B_1 = 2$   $\mu$ T (ideal/preferred);
- b Pulse-train,  $T_{\text{sat}} = 2$  s,  $B_{1\text{rms}} = 2$   $\mu$ T,  $DC_{\text{sat}} = 90$ -100% (preferred);
- c Pulse-train,  $T_{\text{sat}} = 800$ -1000 ms,  $B_{1\text{rms}} = 2$   $\mu$ T,  $DC_{\text{sat}} = 90$ -100%;
- d Pulse-train,  $T_{\text{sat}} = 2$  s,  $B_{1\text{rms}} = 2$   $\mu$ T,  $DC_{\text{sat}} = 50$ %;

Lipid suppression:

- a An effective lipid suppression method (such as SPIR);

Readout (including recovery time):

- a Fast 3D acquisition (in-plane resolution 1.8-2.2 mm; through-plane resolution 3-6 mm);
- b  $T_{\text{rec}} \approx 2T_{1w}$  (tumor  $T_{1w} \approx 1.5$ -1.6 s at 3 T)

#### Acquisition protocols

- a  $B_0$  shimming, preferably 2nd-order shimming, should be done;
- b At least 6-offset/7-point APTw imaging protocols ( $S_0, \pm 3, \pm 3.5$ , and  $\pm 4$  ppm or  $S_0, \pm 3.1, \pm 3.5$ , and  $\pm 3.9$  ppm) should be used. More acquisitions at  $\pm 3.5$  ppm are often needed to increase the APTw SNR. A saturated image at  $\pm 300$  ppm or further from water should be acquired and used as  $S_0$ , with a dummy scan or shot required;
- c Proper water frequency mapping must be acquired

#### Data processing methods

- a Use  $MTR_{\text{asym}}$  (3.5 ppm) as a metric;
- b Use a rainbow color scale ( $\pm 5$ %) leading to a green background with yellow/orange/red hyperintensities and blue hypointensities;
- c Both rainbow color and gray-scale images are stored

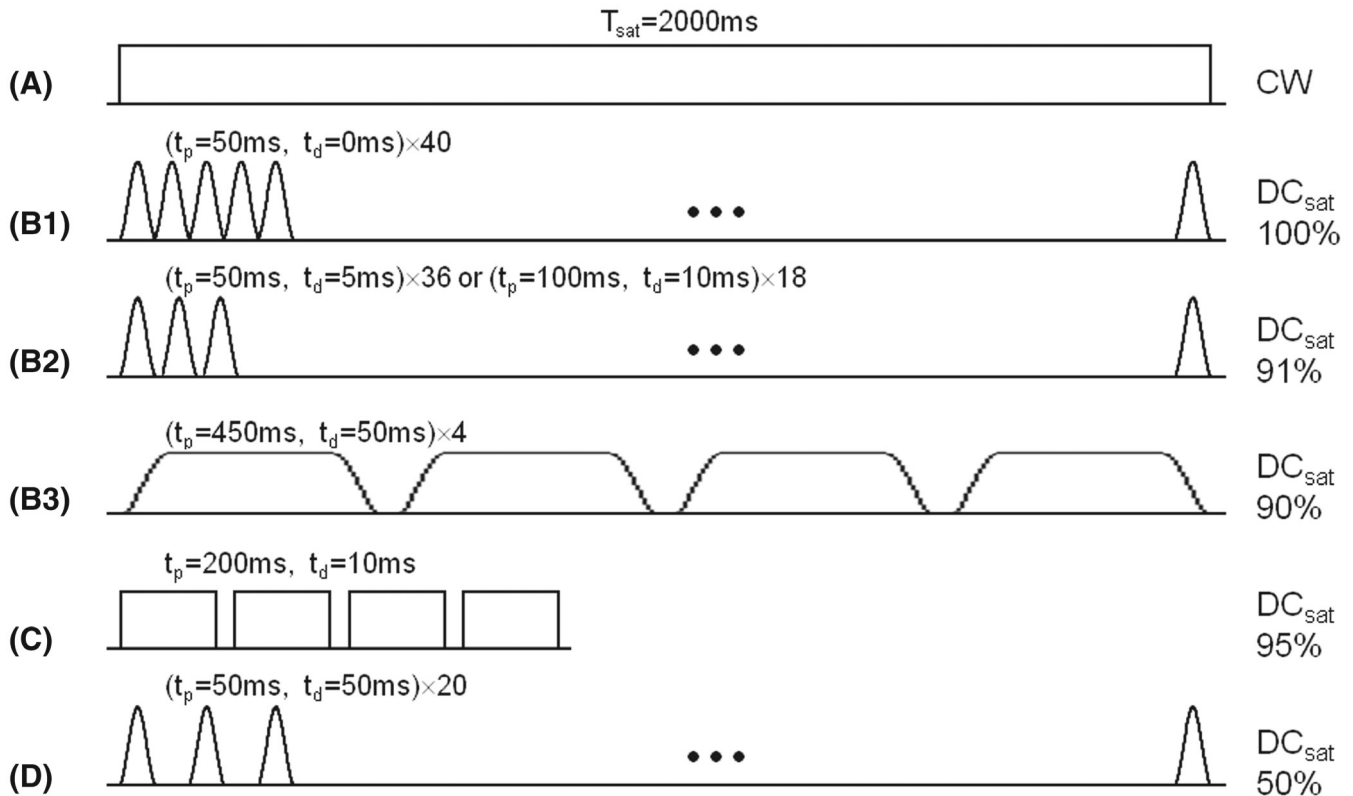


**FIGURE 5** Recommended RF saturation methods for APTw imaging of brain tumors on 3 T clinical MRI scanners. (A) CW RF saturation ( $T_{\text{sat}} = 2$  s,  $B_1 = 2 \mu\text{T}$ ). (B1-B3) Three pulse-train RF saturation examples ( $T_{\text{sat}} = 2$  s,  $B_{1\text{rms}} = 2 \mu\text{T}$ ) with high  $\text{DC}_{\text{sat}} (\geq 90\%)$ , respectively, proposed to be used initially on the Philips system by Keupp et al,<sup>130</sup> on the Siemens system by Zhang et al,<sup>149</sup> and on the GE system by Su et al.<sup>198</sup> Note that (B1) is typically achieved with the time-interleaved pTX technique. Single-lobe sinc-Gaussian or any other saturation pulses may be used in (B1) and (B2), and Fermi pulses in (B3). (C) Shorter pulse-train RF saturation ( $T_{\text{sat}} = 830$  ms,  $B_{1\text{rms}} = 2 \mu\text{T}$ ) with high  $\text{DC}_{\text{sat}} = 95\%$ , which was proposed by Zhu et al.<sup>122</sup> (D) Pulse-train RF saturation ( $T_{\text{sat}} = 2$  s,  $B_{1\text{rms}} = 2 \mu\text{T}$ ) with standard  $\text{DC}_{\text{sat}} = 50\%$ . Single-lobe sinc-Gaussian saturation pulses are used as an example. (C) and (D) are not optimal, but have often been used previously. To exactly reproduce these pre-saturation blocks, find their definition in the pulseseq-CEST library (A: APTw\_000, B2: APTw\_001, C: APTw\_003, D: APTw\_002)<sup>143</sup>

realized with the RF amplifier hardware configuration from all different manufacturers. Time-interleaved pTX is one good option, but not a requirement, because some state-of-the-art RF amplifiers can support a  $\text{DC}_{\text{sat}} > 90\%$  for body coils at the recommended  $B_1$  strength for APTw MRI. The data in Figure 6 confirm that the pulse-train methods in type (b) can provide fairly similar Z-spectra,  $\text{MTR}_{\text{asym}}$  spectra, and APTw images in healthy volunteers from three 3 T MRI scanners of different vendors. When preferred types (a) and (b) are not feasible, we recommend using types (c) or (d). A good example for type (c) is shown in Figure 5C, which has been widely used in brain tumor studies previously.<sup>25,30</sup> A comparison of types (b)-(d) can also be found in Figure 2B. To allow maximal reproducibility, several of the pre-saturation schemes were recently shared in the open-source pulseseq-CEST format<sup>143</sup> (see more details in the caption of Figure 5).

## 4.2 | Lipid suppression

Because APTw images are based on the  $\text{MTR}_{\text{asym}}$  analysis of saturation images at  $\pm 3.5$  ppm from water, lipid artifacts may occur because of the unequal lipid suppression by the saturation pulse at frequencies above and below the water. In addition, when an EPI-type fast imaging readout is used, large lipid ghosting artifacts may interfere with APTw imaging.<sup>144</sup> It should be noted that the issue of fat suppression in the brain is much less severe than in body applications of APT, where partially fat-containing voxels require sophisticated methods to remove fat signals. Normal brain tissue and brain tumors do not contain MR-visible fat components (with the rare exception of teratoma), so lipid artifacts mostly arise from fat outside the brain (skull). Sun et al<sup>144</sup> showed that a spin-echo sequence with a water-based, chemical-shift-selective refocusing pulse could avoid such a lipid artifact in

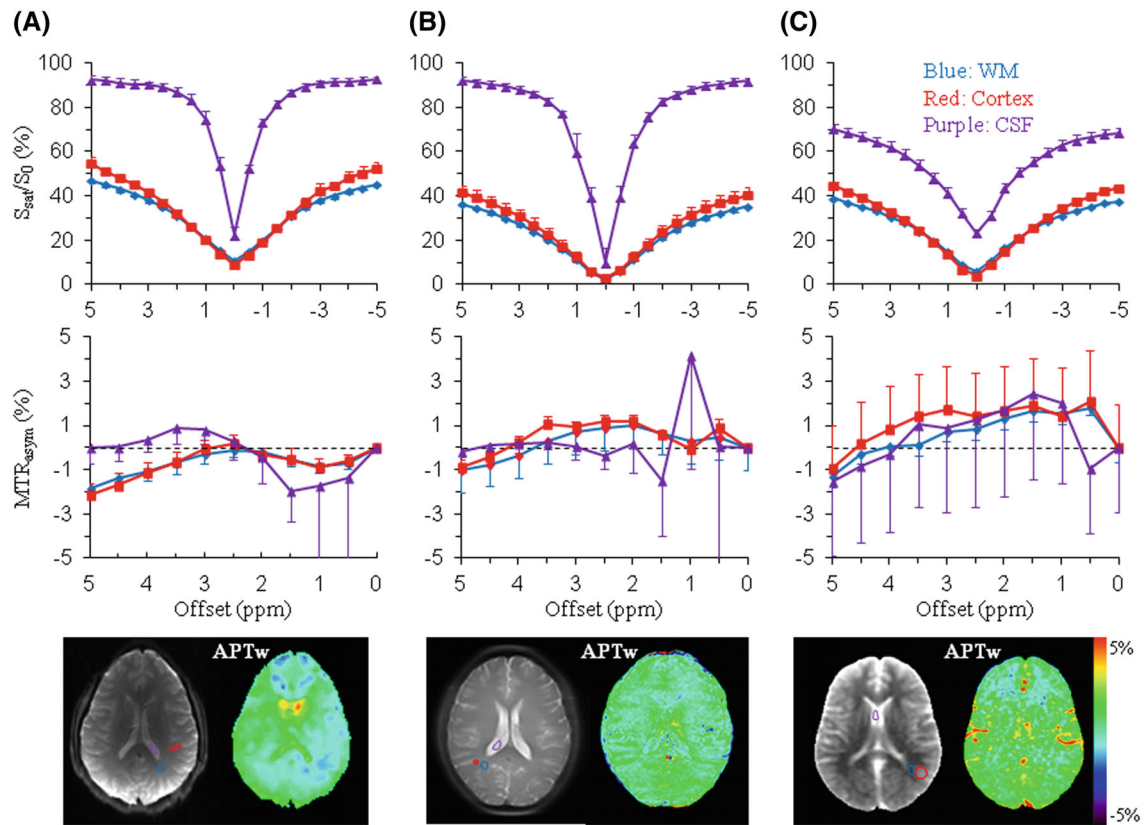


**FIGURE 6** Preliminary results of Z-spectra,  $MTR_{\text{asym}}$  spectra, and APTw images acquired from adult healthy volunteers on a GE 3 T MRI scanner (Discovery MR750) (A), a Philips 3 T MRI scanner (Ingenia) (B), and a Siemens 3 T MRI scanner (Prisma) (C), using the recommended RF saturation methods (Figure 5B3, B1, and B2), respectively. Comparable regions of interest were chosen in white matter (blue lines), cortex (red lines), and cerebrospinal fluid (CSF, purple lines). A single-slice TSE/EPI acquisition was used in (A) and (B), respectively, and the 3D snapshot GRE (7 s per offset) in (C). Similar Z-spectra,  $MTR_{\text{asym}}$  spectra, and APTw images were obtained for the 3 different vendors, particularly for white matter and cortex. Z-spectra and  $MTR_{\text{asym}}$  spectra of CSF show relatively larger standard deviations, which can be attributable to flow-related effects. The use of the fast 3D snapshot GRE in (C) is associated with the larger partial volume effect in the second phase-encoding (head-foot) direction (CSF Z-spectrum) and hyperintense vessel signals (APTw image). Standard deviations are ROI-based (over the number of voxels), and therefore, dominated by the ROI tissue-based spatial inhomogeneity, and provide only coarse insight in the image CNR. Some  $B_0$  centering errors are visible in some of the CSF curves, leading to larger standard deviation close to the water frequency. Unpublished data from Drs. Phillip Zhe Sun and Yin Wu (GE System), Dr. Jinyuan Zhou (Philips System), and Dr. Moritz Zaiss (Siemens System). Studies were approved by the respective local Institutional Review Boards

$MTR_{\text{asym}}$  images. Zhu et al<sup>122</sup> demonstrated that lipid suppression can be effectively achieved using chemical-shift selective removal before acquisition with an asymmetric, frequency-modulated, lipid suppression pulse, followed by a crusher gradient. Several methods have been proposed to suppress strong lipid artifacts in breast CEST imaging.<sup>145–147</sup> Fortunately, it has been shown that the standard spectral pre-saturation inversion-recovery (SPIR) method is generally sufficient for lipid artifact removal in APTw imaging of the brain.<sup>148,149</sup>

### 4.3 | Readout

Clinical application of the APTw MRI approach will be more feasible if fast volumetric imaging acquisition

(<5 min) can be achieved. Both multi-slice and 3D approaches have been used in CEST/APTw imaging. In multi-slice acquisitions, there generally are CEST signal losses because of  $T_{1w}$  relaxation differences based on the order in which the slices are acquired, so corrections may be needed.<sup>150</sup> However, in a 3D acquisition with centric encoding, each line of k-space contributes equally to all reconstructed slices, and differences in saturation caused by differences in  $T_{1w}$  relaxation between slices can be minimized.<sup>122</sup> Therefore, 3D acquisition is preferred for volumetric APTw imaging. For instance, Zhu et al<sup>122</sup> developed a 3D APTw MRI technology that allows fast acquisition on 3 T clinical instruments, using 4 elements of 200 ms with 10 ms space in between ( $DC_{\text{sat}} = 95\%$ ) for gradient- and spin-echo (GRASE)

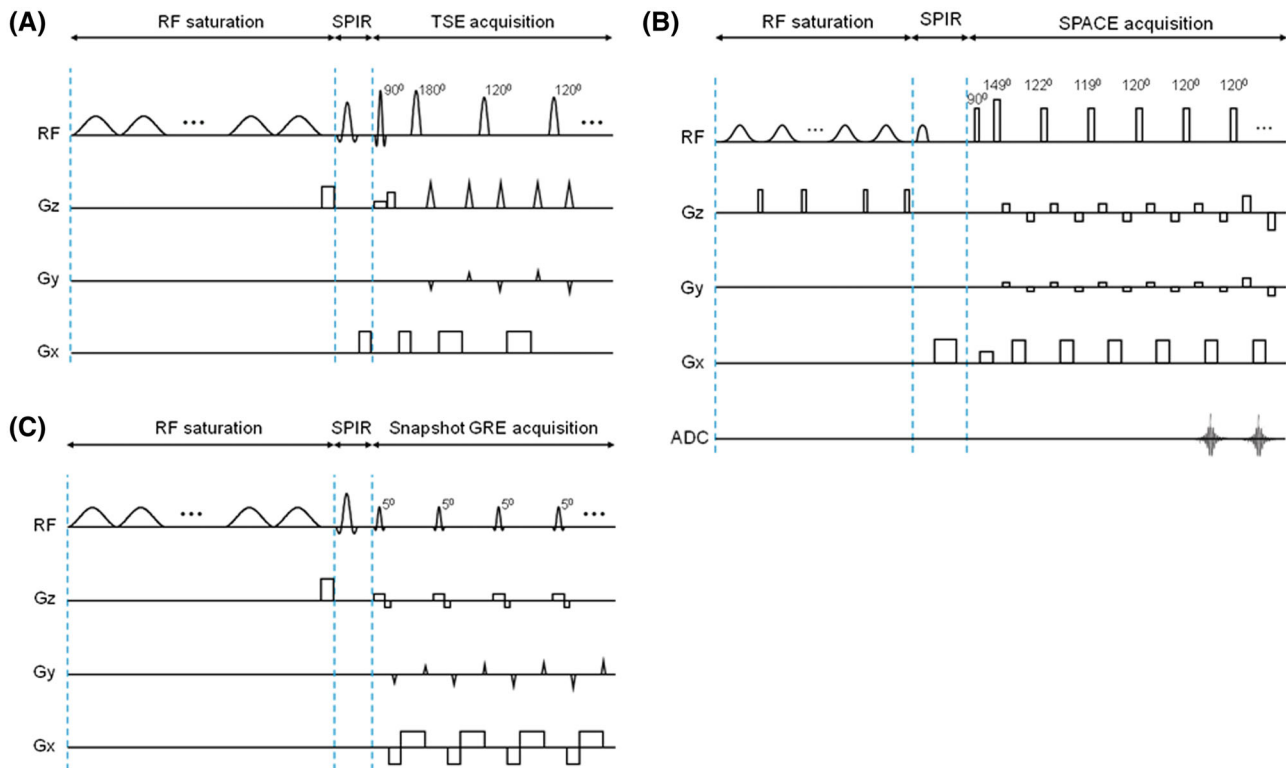


**FIGURE 7** 3D APTw imaging sequence diagrams, all consisting of a pulse-train RF saturation module, a SPIR lipid suppression pulse, and 3D image readout. (A) An example used in the Philips 3 T clinical MRI system. The time-interleaved pTX-based RF saturation module consists of 40 single-lobe sinc-Gaussian saturation pulses (50 ms each,  $T_{\text{sat}} = 2$  s,  $B_{1\text{rms}} = 2$   $\mu$ T,  $\text{DC}_{\text{sat}} = 100\%$ ), corresponding to Figure 5B1. The TSE readout module contains selective excitation and selective/non-selective refocusing pulses ( $120^\circ$ ). (A) Made according to Keupp et al.<sup>130,131,170</sup> (B) An example used in a Siemens 3 T clinical MRI scanner. The RF saturation module consists of a train of 100-ms-long Gaussian pulses with a 10-ms gap in between ( $\text{DC}_{\text{sat}} = 91\%$ ), corresponding to Figure 5B2, and a 5-ms-long, 15-mT/m-strong crusher gradient is applied during the gap period. The SPACE readout module contains non-selective excitation and refocusing pulses. The refocusing part has 4 startup pulses with flip angles of  $149^\circ$ ,  $122^\circ$ ,  $119^\circ$ , and  $120^\circ$ , and then executes constant  $120^\circ$  pulses. (B) Reproduced with permission from Zhang et al.<sup>149</sup> (C) An example of the snapshot GRE CEST used in a Siemens 3 T clinical MRI scanner. The RF saturation module consists of a train of 36 50-ms-long Gaussian pulses with a 5-ms gap in between ( $\text{DC}_{\text{sat}} = 91\%$ ), corresponding to Figure 5B2, and a 2-ms-long, 15-mT/m-strong crusher gradient is applied after the preparation period. The snapshot GRE readout module contains slab-selective, low flip-angle excitation pulses of  $5^\circ$ - $7^\circ$ . (C) Made according to Zaiss et al.<sup>157</sup> and Herz et al.<sup>129</sup>

imaging with adiabatic lipid suppression pulses. This sequence has been applied successfully to clinical studies at many sites.<sup>30,151</sup>

Volumetric APTw MRI currently requires a scan time of 3 to 10 min, because of the use of multiple RF saturation frequencies (to correct for the  $B_0$  inhomogeneity) and multiple acquisitions (to increase the SNR). Various acceleration approaches and fast imaging acquisition techniques have been used to accelerate CEST/APTw imaging (Figure 7), including SENSE,<sup>152,153</sup> GRAPPA,<sup>154</sup> controlled aliasing in parallel imaging results in higher acceleration (CAIPIRINHA),<sup>155</sup> GRASE readout,<sup>122</sup> turbo-spin-echo (TSE) readout<sup>22,23,156</sup> (including sampling perfection with application-optimized contrasts by using different flip angle evolutions [SPACE]),<sup>149</sup> and a gradient-echo (GRE)-based snapshot approach.<sup>157-159</sup> The combination of 3D TSE readout with time-interleaved

pTX saturation provides a fast and more sensitive 3D APTw imaging sequence (Figure 7A), which was the method used in the first commercial APTw imaging sequence on Philips 3 T MRI scanners.<sup>60,61</sup> In addition, several novel undersampling acquisition and reconstruction approaches (including keyhole, spectroscopy with linear algebraic modeling, compressed sensing, and deep learning)<sup>160-165</sup> have been used successfully to accelerate CEST/APTw acquisitions. The reconstruction-oriented, reduced k-space acquisition requires more advanced data processing, but this can all be automated on the scanners (including compressed sensing-based image reconstruction and  $B_0$  inhomogeneity correction)<sup>60,61</sup> to streamline the clinical workflow.

Based on previous studies, a fast 3D acquisition technique (in-plane resolution 1.8-2.2 mm; through-plane resolution 3-6 mm), integrated with a feasible, optimized



RF saturation scheme and an effective lipid suppression method, and is recommended for brain tumor APTw imaging on 3 T clinical MRI scanners (Table 4).  $T_{\text{rec}}$  or TR is generally limited by the SAR, and we suggest using  $T_{\text{rec}} \approx 2T_{1w}$  (tumor  $T_{1w} \approx 1.5\text{--}1.6$  s at 3 T).<sup>118,119</sup> GRASE,<sup>122</sup> TSE,<sup>61</sup> SPACE,<sup>149</sup> and GRE<sup>157–159</sup> have widely been used in previous studies of brain tumor APTw imaging and are among the candidate readout sequences. However, we recommend retaining some flexibility for the 3D readout module, currently, because the choice of this pulse sequence component does not affect the APTw contrast per se.

## 5 | ACQUISITION PROTOCOLS

The minimum data required to calculate  $MTR_{\text{asym}}$  is related to a 2-offset ( $\pm 3.5$  ppm) APTw imaging protocol. However,  $MTR_{\text{asym}}$  analysis is complicated by  $B_0$  frequency inhomogeneity and scanner instability, which causes spatio-temporal resonance frequency variations. The 2-offset protocol is highly susceptible to  $B_0$  variations between voxels, which can be problematic near air-tissue interfaces, even with up to 2nd-order shimming.<sup>122</sup> Two kinds of APT imaging acquisition protocols have been reported in the literature that address this issue (Tables 2 and 3): acquiring a full Z-spectrum consisting of

downfield and upfield frequency offsets from the water resonance, or acquiring limited frequency offsets at and around  $\pm 3.5$  ppm, plus a  $\Delta B_0$  map for frequency offset referencing. A full Z-spectrum is often acquired for research purposes and allows for correction of  $B_0$  variations because it includes samples near water and amide resonances. The APTw signal is known to appear at the offset of 3.5 ppm; therefore, only limited offsets at and around  $\pm 3.5$  ppm need to be acquired.<sup>12</sup> To have the possibility to correct for  $B_0$  differences on a voxel-by-voxel basis, it is necessary to acquire multiple offsets at and around  $\pm 3.5$  ppm. The  $\Delta B_0$  map is often obtained using an extra, more time-efficient scan, such as the widely used water saturation shift referencing (WASSR)<sup>166</sup> or GRE phase-based methods.<sup>156,167</sup> According to the literature,<sup>122</sup> the  $B_0$  inhomogeneity in the brain is typically less than 20 Hz and up to 100 Hz near air-tissue interfaces (ears, sinuses) at 3 T. With a  $\Delta B_0$  map available, it has been shown that a 6-offset APTw imaging protocol ( $\pm 3$ ,  $\pm 3.5$ , and  $\pm 4$  ppm) with 2-to-4 acquisitions at  $\pm 3.5$  ppm (Figure 8A), can provide  $B_0$  inhomogeneity-corrected APTw images of sufficient SNR.<sup>23</sup> This minimal Z-spectrum data acquisition allows 3D full brain imaging within clinically acceptable acquisition times (e.g., <5 min). More acquisitions at  $\pm 3.5$  ppm can be used to increase the SNR. Of course, a relatively larger offset interval (e.g.,  $\pm 2.75$ ,  $\pm 3.5$ ,  $\pm 4.25$  ppm) or extra offsets (e.g.,  $\pm 2.5$ ,  $\pm 3$ ,  $\pm 3.5$ ,  $\pm 4$ ,  $\pm 4.5$  ppm) may be used

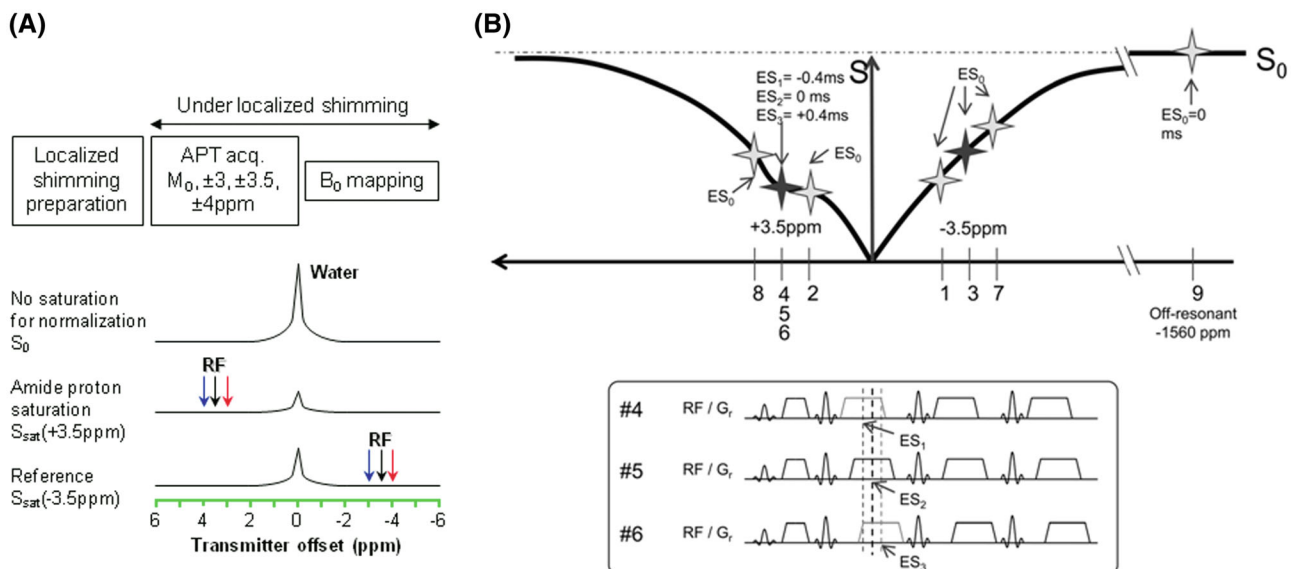


**FIGURE 8** (A) A commonly used 6-offset APTw protocol. During the preparation, localized shimming is performed. The optimal shim parameters and scanner's center frequency are determined and applied to the subsequent APTw data acquisition and  $\Delta B_0$  mapping scans. During the APTw data acquisition, extra offsets ( $\pm 3$ ,  $\pm 4$  ppm) are acquired to correct for spatial and temporal  $B_0$  inhomogeneities. Reproduced with permission from Zhou et al.<sup>23</sup> (B) An APT-Dixon method. The imaging is performed at frequency offsets  $\pm 3.1$ ,  $\pm 3.5$ ,  $\pm 3.9$ , and  $-1560$  ppm ( $S_0$ ). Image acquisition is repeated 3 times at  $+3.5$  ppm. Acquisition windows and readout gradients are shifted (echo-shift, [ES]) by  $+0.4$  ms ( $ES_1$ ),  $0$  ms ( $ES_2$ ), and  $-0.4$  ms ( $ES_3$ ) in each acquisition at  $+3.5$  ppm for Dixon-type  $\Delta B_0$  mapping. Reproduced with permission from Togao et al.<sup>170</sup>

when large  $B_0$  inhomogeneities exist.<sup>23,168</sup> The tradeoffs for these are larger data interpolation errors (see next section) and more scan time, respectively.

Recently, a number of novel methods have been proposed to correct  $B_0/B_1$  field inhomogeneity or frequency drift in clinical CEST/APTw imaging at both 3 T and 7 T.<sup>169–178</sup> Keupp et al<sup>169,170</sup> developed a so-called CEST-Dixon method at 3 T that can map the intrinsic  $B_0$  inhomogeneity using echo shifts during the APTw acquisition (Figure 8B), concluding that this self-corrected method is more robust than separate  $B_0$  mapping approaches. Schuenke et al<sup>171</sup> proposed the water shift and  $B_1$  (WASABI) method that can yield simultaneous  $B_0$  and  $B_1$  mapping within about 2 min at 3 T and 7 T. The  $B_1$  variations in the brain at 3 T are typically within  $\pm 10\%$  and can be up to  $\pm 30\%$  in some regions, such as in the infratentorial region and at the superior part of the brain.<sup>159</sup> Theoretically,  $B_1$  inhomogeneity affects APTw signal when different brain regions experience varying amounts of saturation. For example, the saturation efficiency  $\alpha$  in Equation (1) is a function of  $B_1$ , and spillover/MTC dilution effects change with  $B_1$ .<sup>67</sup> At 3 T, when a body coil is used, these effects taken together may not be sufficient to substantially affect APTw contrast within most brain slices (Figure 6). However, this may be an issue only in the infratentorial and superior brain regions, and further assessments are needed. Technically, if available, parallel transmit and  $B_1$  shimming, as well as  $B_1$  inhomogeneity corrections during processing (from  $B_1$  mapping), should be used to reduce the possible issue. Poblador Rodriguez et al<sup>177</sup> recently compared several static and dynamic  $\Delta B_0$  mapping methods for correcting CEST MRI in the presence of temporal  $B_0$  field variations at 7 T. The results indicated that, in the presence of frequency drift, the 3 dynamic methods (which integrate  $\Delta B_0$  mapping into the CEST measurement) had significantly improved  $\Delta B_0$ -correction performance over established static methods. Self-corrected CEST-GRE-2TE (using phase data directly generated by double-echo GRE readout), comparable to CEST-Dixon, was the most accurate and straightforward sequence to implement.

The APTw acquisition protocol currently recommended for brain tumors on 3 T clinical MRI scanners is listed in Table 4. We recommend the acquisition of at least 6 offsets and an unsaturated image ( $S_0$ ,  $\pm 3$ ,  $\pm 3.5$ ,  $\pm 4$  ppm, or  $S_0$ ,  $\pm 3.1$ ,  $\pm 3.5$ ,  $\pm 3.9$  ppm), in combination with  $B_0$  shimming (2nd order preferred) and a  $B_0$  shift reference. Further offsets can be applied, if a larger  $B_0$  inhomogeneity is expected. Because the APTw effect in vivo is often small (2–4% of the water intensity in tumor), multiple acquisitions are often needed to increase the APTw SNR. We recommend that  $S_{\text{sat}}(\pm 3.5 \text{ ppm})$  images

should have an SNR of at least  $\sim 50$ , corresponding to 2-to-3 acquisitions for the TSE readout, with an in-plane spatial resolution of about 1.8 to 2.2 mm and a through-plane resolution of 3 to 6 mm. Notably,  $S_0$  without RF saturation should be acquired using the same TR as saturated images. It is acceptable that a saturated image at a very large offset is used as  $S_0$ , which avoids potential drift effects with RF power changes. In this case,  $\pm 300$  ppm or further from water should be chosen. At least 1 dummy scan or shot is required for the single-shot or multi-shot acquisition, respectively. Finally, an intrinsically/dynamically referenced  $\Delta B_0$ -correction method (such as CEST-Dixon or CEST-GRE-2TE)<sup>128,129,177</sup> is a good option to correct for  $B_0$  variations, but a separate  $\Delta B_0$  mapping approach is generally acceptable at 3 T. For the latter, it is, of course, important to run the  $\Delta B_0$  mapping and APTw scans under the same shimming and ideally in immediate succession, because of potential  $B_0$  drift effects (Figure 8A). The approaches and parameters suggested in Table 4 allow for the greatest degree of flexibility in the application of APTw imaging to multi-center clinical trials for the assessment of brain tumors and novel therapies.

## 6 | DATA PROCESSING

Different data processing approaches have been proposed to quantify the APT effect in vivo. Examples are the widely used  $\text{MTR}_{\text{asym}}$  analysis,<sup>179</sup> the 3-offset method,<sup>75</sup> and the extrapolated semi-solid magnetization transfer reference (EMR) method,<sup>95,96</sup> which were designed to, as much as possible, remove the DS and MTC background signals based on a reference signal. Other approaches include various model-based,  $Z$ -spectral fitting approaches, such as multi-pool Lorentzian fitting<sup>180–182</sup> or multi-pool Bloch-McConnell equation fitting.<sup>183,184</sup> These often allow a more specific CEST quantification and provide the ability to quantify multiple CEST parameters. The most suitable APT analysis method may depend on the setting of RF saturation amplitudes. At relatively low saturation amplitudes ( $< 1 \mu\text{T}$ ), APT and rNOE peaks are often distinguishable and relatively easy to fit. However, at  $2 \mu\text{T}$  recommended for brain tumor imaging at 3 T, the distinct APT signal at 3.5 ppm is often invisible (because of a large saturation bandwidth on the order of ppm)<sup>94</sup> and the model-based fitting approaches, designed to separate out more pure APT effects, may not work well. Recently, a quasi-steady-state (QUASS) CEST analysis method was developed to account for the effects of finite saturation time and relaxation delay, which may facilitate more robust CEST quantification of individual resonances.<sup>185,186</sup> Here, we focus on the consensus on APTw imaging using  $\text{MTR}_{\text{asym}}$  analysis, whereas other

quantification approaches will require a separate evaluation and consensus.

Notably, in addition to its simplicity and speed,  $MTR_{\text{asym}}$ -based APTw imaging at 2  $\mu\text{T}$  has some other useful characteristics that are not directly related to amide proton exchange properties, such as the close-to-0 APTw signal in healthy tissue and the coarse  $T_{1w}$  independence, as discussed above. According to Table 2, when a  $B_{1\text{rms}}$  of 2  $\mu\text{T}$  and a  $T_{\text{sat}}$  of 2 s are used on 3 T MRI scanners, very similar APTw intensities or contrasts can be observed from different vendors/sites (grade-4/3/2 glioma APTw contrast = 4.0%/2.2%/1.0% on GE; grade-4/3/2 glioma APTw signal = 4.1%/3.2%/2.1% on Philips; high-grade glioma APTw signal = 3.5% on Philips),<sup>54,26,164</sup> ranging approximately from 1% to 4% in solid tumors of different grades. The  $MTR_{\text{asym}}$  (3.5 ppm) or APTw metric has, therefore, become the basis of the first commercial APTw imaging sequence on 3 T clinical MRI scanners.<sup>60</sup>

Based on previous studies, we recommend  $MTR_{\text{asym}}$  (3.5 ppm,  $B_{1\text{rms}} = 2 \mu\text{T}$ ,  $T_{\text{sat}} > 0.8 \text{ s}$ ,  $DC_{\text{sat}} \geq 50\%$ ) for brain tumor APTw imaging on 3 T clinical MRI scanners (Table 4). Using the recommended 6-offset acquisition protocol and estimate of  $B_0$  offset, the equivalent value for the signal at  $\pm 3.5$  ppm should be calculated using interpolation (linear or Lagrange interpolation being suitable with the small number of sample points) and  $MTR_{\text{asym}}$  (3.5 ppm) calculated from these values.<sup>26,148,151</sup> Most APTw images have been displayed historically using a rainbow color scale. When the recommended  $B_1$  and saturation time values are used, this often leads to a green background in normal brain regions with positive, yellow/orange/red hyperintensities in high-grade tumors (Figure 9) and negative, blue hypointensities in ischemic tissue.<sup>142</sup> We, therefore, recommend that the results should be displayed on MRI scanner consoles in a window of  $\pm 5\%$ , with a specific rainbow colorbar (no. 013), defined by Interactive Data Language (IDL; Harris Geospatial Solutions, Broomfield, CO),<sup>187,188</sup> to visually cover all possible APTw signal changes seen in different clinical applications, and that both rainbow color and gray-scale images are stored. In addition, to enable comparison of APTw images to previous published data, we suggest that the results should be displayed in publications using this colorbar and window. Nevertheless, we understand that radiologists may choose windows and levels themselves in reading rooms using different post-processing solutions and may use gray-scale or any color scales that they prefer for their specific clinical study with APTw imaging. Although radiologists usually prefer the rainbow scale, it is important to point out that it is increasingly recognized that this scale is not very suitable for color-blind people and that the sharp color transitions may be misleading.<sup>189</sup> We encourage experimentation with the use of perceptually uniform

sequential colorbars for APTw imaging in the future. Because of a lack of published data with such scales, we can currently not make a consensus recommendation about this.

## 7 | DATA INTERPRETATION

As is typical for all MRI approaches, there can be false-positive and false-negative findings because of low SNR. This certainly applies to CEST MRI, including APTw imaging, which detects changes in the range of a few percent of the water MRI signal. Consequently, the APTw MRI approach, based on difference images, is susceptible to motion and  $B_0$  shifts that may cause artifacts in the APTw images. Although low SNR, together with motion, can average out small hypo- or hyperintensities, strong motion artifacts can also lead to false hyper- or hypo-intensities, as previously shown for dynamic CEST studies.<sup>190</sup> It has been reported on clinical scanners, with a saturation time of 2 s and a  $B_1$  amplitude of 2  $\mu\text{T}$ , that the repeatability of the APTw signal was excellent in supratentorial locations, but it was poor in infratentorial locations because of severe  $B_0$  inhomogeneity and susceptibility that affect the APTw signal.<sup>163,164</sup> In addition, as discussed in "Acquisition Protocols," the  $B_1$  inhomogeneity can be up to  $\pm 30\%$  in the infratentorial and superior regions of the brain, which may affect the APTw signal. Therefore, interpretation of APTw imaging must include possible SNR,  $B_0/B_1$  inhomogeneity, and motion influences, or rule these out at the acquisition or post-processing stage, which may be possible with future developments.

Although APTw imaging is useful for brain tumor evaluation, there are pitfalls for APTw image interpretation. In addition to artifacts because of motion and  $B_0$  alterations, areas of large liquefactive necrosis, hemorrhage, or large vessels typically demonstrate high APTw signals and should not be mistaken as viable tumor.<sup>11</sup> Figure 10 gives several representative images of liquefactive necrosis and hemorrhage at different stages. Careful interpretation is needed with post-operative-stage tumors with the surgical cavity filled with proteinaceous fluid, unless a fluid suppression method is used (Figure 10C and D).<sup>56,111</sup> To distinguish between viable tumor and proteinaceous fluid, APTw images should generally be interpreted together with anatomic MRI (such as  $T_{2w}$ , fluid-attenuated inversion recovery (FLAIR), and pre- and post-contrast  $T_{1w}$ ), SWI, diffusion, and perfusion (including dynamic susceptibility contrast-enhanced and dynamic contrast-enhanced) MRI sequences that are acquired during routine clinical tumor protocols. This comparison helps, on one hand, to recognize and assign non-tumorous signals and potential artifacts on APTw

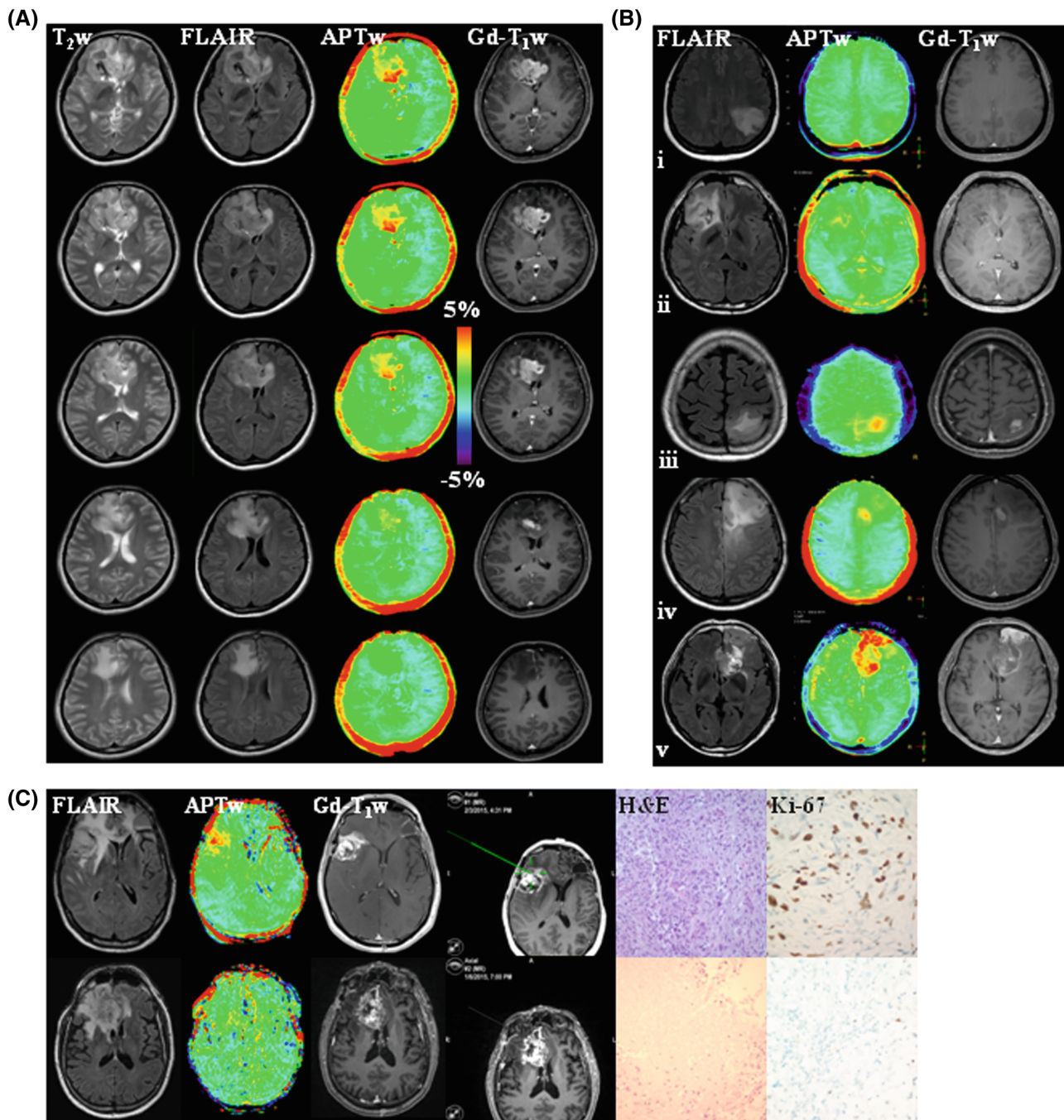


**FIGURE 9** (A) An example of anatomic and APTw MR images for a patient with glioblastoma, isocitrate dehydrogenase (IDH) wild-type. APTw images show hyperintensity in the Gd-enhancing area, compared to the contralateral brain area. Five of 10 slices are shown. Unpublished data provided by Dr. Osamu Togao. The study was approved by the local institutional review board. (B) Five examples of anatomic and APTw MR images for patients with astrocytoma, IDH-mutant, grade 2 (row i); oligodendroglioma, IDH-mutant, 1p/19q codeletion, grade 2 (row ii); astrocytoma, IDH-mutant, grade 3 (row iii); astrocytoma, IDH-mutant, grade 4 (row iv); and glioblastoma, IDH-wildtype, grade 4 (row v). Grade 3 or 4 gliomas typically show Gd enhancement and intermediate to high APTw hyperintensity. The 2021 World Health Organization classification of brain tumors was used. Unpublished data provided by Dr. Ji Eun Park. The study was approved by the local institutional review board. The recommended RF saturation method (Figure 5B1), 3D TSE readout, and APT-Dixon method (Figure 8B) were used in (A) and (B). (C) Two examples of anatomic and APTw MR images, biopsied sites, and histology images from an APTw image-guided stereotactic biopsy study, using the RF saturation method in Figure 5C, a 3D GRASE readout, and the 6-offset APTw acquisition protocol from Figure 8A. (Top) A gliosarcoma patient with tumor recurrence, showing heterogeneous substantial APTw hyperintensity in the Gd-enhancing area. The biopsied site marked by a screenshot had a high APTw signal (3.42%). (Bottom) A glioblastoma patient with treatment effect, showing homogeneous isointensity to minimal APTw hyperintensity in the gadolinium-enhancing area. The biopsied site had a relatively low APTw signal (0.87%). Reproduced with permission from Jiang et al.<sup>43</sup>

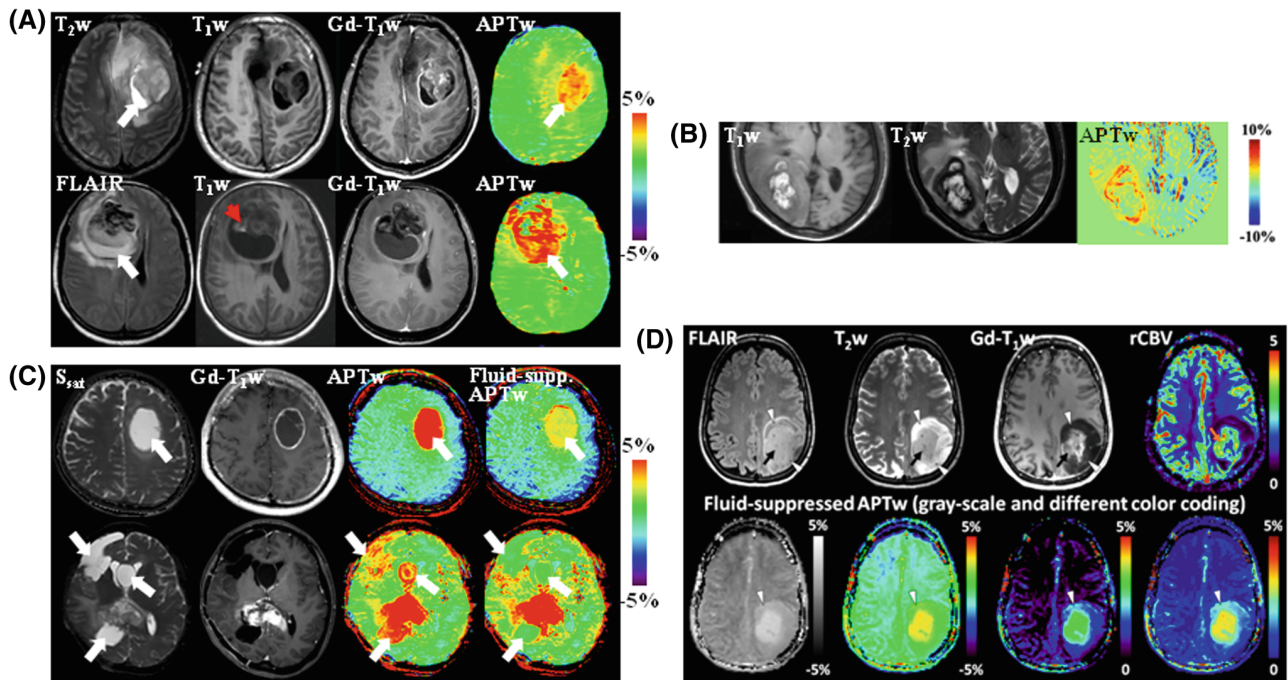


**FIGURE 10** (A) Anatomic and APTw MR images for 2 patients with glioblastoma. (Top) An area of liquefactive necrosis (white arrow) is evident on standard anatomic MRI sequences. The APTw image shows that both the Gd-enhancing tumor core and the proteinaceous fluid-filled cavity (white arrow) have high APTw signal intensities. (Bottom) There is a large cavity filled with liquefactive necrosis (high FLAIR; white arrow) inside the tumor mass. T<sub>1</sub>w image demonstrates a small region of high signal intensities (red arrowhead) that is characteristic of hemorrhage. Both the tumor core and the liquefactive necrosis generally have high APTw signals, whereas the clot (red arrowhead) has a low APTw signal. Reproduced with permission from Wen et al.<sup>24</sup> (B) MRI of hemorrhage metastasis. At the periphery, the lesion shows isointensity on the T<sub>1</sub>w image and hypointensity on the T<sub>2</sub>w image, both consistent with acute hemorrhage. However, the central portion of the lesion shows hyperintensity on both T<sub>1</sub>w and T<sub>2</sub>w images, consistent with late subacute hemorrhage. The APTw image demonstrates a higher signal in the acute hemorrhage region than in the subacute hemorrhage region. Reproduced with permission from Jeong et al.<sup>114</sup> (C) Standard APTw and fluid-suppressed APTw MR images for 2 patients with glioblastoma. (Top) A tumor with large central fluid content showing only thin rim enhancement after fluid suppression. (Bottom) A complex case with the significant cleanup of fluid APTw signals with fluid suppression. Reproduced with permission from Keupp and Togao.<sup>111</sup> (D) Anatomic, dynamic susceptibility contrast-enhanced perfusion-weighted, and fluid-suppressed APTw MR images in a patient with a histologically confirmed astrocytoma, IDH-mutant, grade 4. The anatomic images demonstrate a heterogeneous lesion with a rather solid central and well-enhancing part (black arrows), a peripheral compartment (arrowheads), and some T<sub>2</sub>w/FLAIR mismatch without overt enhancement. The area of strong enhancement also demonstrates strong neo-vascularization as is evident on the leakage-corrected relative cerebral blood volume (rCBV) map (orange arrow), whereas the peripheral lesion shows a very low vascularization index. The APTw images in different color-coding show significantly elevated signal in the enhancing tumor, suggesting clearly high-grade features. Interestingly, the anterior rim zone, along with a halo surrounding the enhancing area, demonstrates mildly elevated APTw signal (arrowheads) that indicates likely high-grade tumor characteristics, which are not captured by the perfusion-weighted MRI. The APTw image appears to provide a more accurate functional tumor mapping than the rCBV map in this case. Unpublished data provided by Drs. Sotirios Bisdas and Laura Mancini (University College London Hospitals NHS Foundation Trust and UCL Queen Square Institute of Neurology) from an ongoing study approved by the Institutional Review Board and the local ethics committee. The data were acquired on a Siemens 3 T Prisma scanner, using a 3D APTw protocol ( $DC_{sat} = 91\%$ ,  $B_{1rms} = 2 \mu T$ ,  $T_{sat} = 2 s$ ) and water shift and B<sub>1</sub> for B<sub>0</sub> and B<sub>1</sub> mapping. Perfusion, water shift and B<sub>1</sub>, and APTw data were processed in Olea Sphere 3.0 software (Olea Medical, La Ciotat, France)

images and, on the other hand, to identify tumor viability characteristics, which are not captured by the structural and perfusion-weighted MRI (Figure 10D). The information provided by APTw MRI should be regarded as complementary to existing approaches, further extending the repertoire of diagnostic tools in radiology. Finally, and importantly, the selection of the color scheme in the APTw images can affect the interpretability of the

information contained, as discussed in “Data Processing.” Advanced post-processing solutions suited for APTw imaging can offer different color scales and windows, including perfusion-like color ranges, which may be more familiar to the radiologist and, therefore, more easily readable (Figure 10D).

As discussed in “Pulse Sequences,” a correction for T<sub>1</sub>w changes is not necessary for APTw imaging of brain

tumors at 2  $\mu\text{T}$  on clinical 3 T scanners.  $T_{1w}$  values decrease after Gd injection, especially in Gd-enhancing regions that are of importance for tumor assessment. The Gd may remain there for a longer time, whereas it may clear faster from other tumor regions, leading to  $T_1$  heterogeneity in the tissue. Shorter  $T_{1w}$  causes a reduced signal buildup in saturation transfer that leads to the region-dependence of quantification because of  $T_{1w}$  heterogeneity.<sup>103</sup> This could be corrected for if  $T_{1w}$  could be known; however, because of the change in  $T_{1w}$  over time with Gd concentration in the region,  $T_{1w}$  mapping after Gd is actually difficult. We, therefore, do not recommend APTw MRI after Gd, but if it is acquired, we suggest adding a note for this to help the interpretation.<sup>101,102</sup> Other metrics with relaxation compensation ability have been suggested,<sup>101,102</sup> and a test to compensate for Gd-induced  $T_1$  changes on injection was performed in an animal tumor model.<sup>191</sup> However, how these findings translate from animals to humans and from the sole amide CEST signal used to  $MTR_{\text{asym}}$  is not yet clear. It is, therefore, not part of this guidelines paper.

## 8 | CONCLUSIONS AND REMARKS

This paper reviews and recommends the currently optimized APTw approaches at 3 T with an attempt to standardize this imaging technology in the clinical setting, and focus on APTw imaging applications to brain tumors (Tables 4 and 5). When the preferred pulse-train method ( $B_{\text{rms}} = 2 \mu\text{T}$ ,  $T_{\text{sat}} = 2 \text{ s}$ ) is applied to healthy volunteers, comparable Z-spectra and  $MTR_{\text{asym}}$  spectra can be obtained from the 3 T MRI scanners of the 3

main manufacturers. In addition, when using the recommended saturation sequences, currently published data from patients with brain tumors show that very similar APTw intensities or contrasts are observed for data from different vendors. We expect that these recommendations will become the first guidelines for APTw imaging of brain tumors on 3 T MRI systems from different vendors. When implemented, more medical centers will be able to use the same or comparable techniques in investigating the added clinical value of APTw MRI in larger independent patient cohorts and ultimately lead to biomarker status of this contrast for brain tumors. Reducing variability across vendors, sites, patients, and time will improve value and practicality of APTw imaging as a quantitative imaging biomarker that is consistent with the mission of the quantitative imaging biomarkers alliance (QIBA).<sup>192</sup>

In addition to the brain tumor applications described above, APTw MRI has been applied to various neurological disorders and other diseases in the clinical setting. Notably, the extension of APTw MRI from the brain to other body regions is complicated by increased  $B_0$  inhomogeneity, motion, and increased lipid contamination, which often lead to inferior imaging quality for many patients. Undoubtedly, APTw imaging methods must be optimized and standardized separately for each of these applications, and consensus recommendations are not possible at this time. In addition to 3 T, APTw imaging applications to patients with brain tumors have been studied at 7 T<sup>102,193,194</sup> and 1.5 T,<sup>195,196</sup> with the latter being important clinically. Theoretically, the extension to lower magnetic field is straightforward; however, the increase in

TABLE 5 Tips for using APTw imaging in the clinical setting

1	Check APTw imaging sequence parameters and test them with a healthy subject on sequence installation, after any scanner upgrade, and on a regular basis
2	Position the head of the subject at the center of RF coil, immobilize as much as possible with padding, and advise the subject to keep stable during the scanning
3	Acquire $T_2$ -weighted and FLAIR images first, and, if not the whole brain is acquired, select an appropriate target volume for APTw imaging. It is also helpful to check the location of the lesion in advance from the most recent MR images of the subject, if available
4	If a separate $\Delta B_0$ mapping approach is used as reference for the APTw scan, turn off its pre-scan to avoid changes in shim and frequency offset settings
5	Acquire APTw MRI before Gd contrast administration. If it is acquired after, add a note for this to help the interpretation
6	Ask whether APTw imaging provide complementary information to the standard MRI protocol including anatomic sequences
7	APTw images should be interpreted together with routine clinical MR images, and areas of large liquefactive necrosis, hemorrhage, or large vessels that typically demonstrate high APTw signals should be identified. Interpretation must also assess possible SNR, $\Delta B_0$ , and motion influences. The infratentorial location is challenged in repeatability; therefore, tumors in the infratentorial location, especially in the brainstem, must be interpreted carefully
8	The recommendations in this work refer specifically to brain tumor imaging. Applications for other diseases and in other organs may require adaption of APTw MRI sequence parameters and acquisition protocol

background interference (smaller frequency range in Hz) would affect the APTw MRI signal, and there is currently insufficient knowledge for a consensus. APTw imaging for other applications is still in its infancy. A continued effort to explore new APTw MRI pulse sequences, data acquisition protocols, and data processing methods is needed, particularly for neurological disorders other than brain tumors and various body diseases. We expect that significant advances will be achieved and updated new recommendations will be proposed within the next 5 years or so.





## ACKNOWLEDGMENTS









We thank Drs. Weiqiang Dou, Mitsuharu Miyoshi, and Bin Wu (GE Healthcare), Drs. Queenie Chan, Weibo Chen, Shuguang Hu, Jochen Keupp, Eunju Kim, Kim van de Ven, Michael Wyss, Masami Yoneyama, Xuna Zhao, and Yansong Zhao (Philips Healthcare), Drs. Yi-Cheng Hsu, Patrick Liebig, Li Pan, Benjamin Schmitt and Yi Sun (Siemens Healthineers), and Dr. Stefano Casagrande (Olea Medical) for help and suggestions over the years. We thank Drs. Sotirios Bisdas and Laura Mancini (University College London Hospitals NHS Foundation Trust and UCL Queen Square Institute of Neurology, London, United Kingdom) for kindly providing their unpublished Figure 10D and related explanation. We also thank Dr. Wilfred W. Lam (Sunnybrook Research Institute) for many helpful discussions. Funding information: National Institutes of Health, Grant/Award Numbers: R01CA228188 and R01AG069179 (to J.Z.); R37CA248077 (to S.J.); P41EB029460 (to R.R.); P41EB015909 and R01EB015032 (to P.C.M.v.Z.); Swedish Research Council, Grant Numbers: 2015-04170 (to L.K.); 2019-01162 (to P.C.S.); Swedish Cancer Society, Grant Numbers: CAN 2015/251 and CAN 2018/550 (to L.K.); CAN 2018/468 (to P.C.S.); National Research Foundation of Korea (NRF), Grant number: 2014R1A1A1002716 (to S.S.A.); German Research Foundation (DFG), Grant number: 445704496 (to D.P.).

## CONFLICT OF INTEREST

J.Z. and P.C.M.v.Z. are paid lecturers for Philips and are the inventors of technology (including APTw MRI) licensed to Philips. P.C.M.v.Z. also has research support from Philips Healthcare. These arrangements have been approved by Johns Hopkins University in accordance with its conflict-of-interest policies.

## ORCID

Jinyuan Zhou  <https://orcid.org/0000-0002-6684-7920>  
 Linda Knutsson  <https://orcid.org/0000-0002-4263-113X>  
 Phillip Zhe Sun  <https://orcid.org/0000-0003-4872-1192>  
 Steffen Goerke  <https://orcid.org/0000-0002-0684-2423>

Hye-Young Heo  <https://orcid.org/0000-0002-7297-2015>  
 Tao Jin  <https://orcid.org/0000-0003-2912-3517>  
 Daniel Paech  <https://orcid.org/0000-0001-5755-6833>  
 Mark D. Pagel  <https://orcid.org/0000-0002-8109-3995>  
 Moriel Vandsburger  <https://orcid.org/0000-0003-4052-205X>  
 Yin Wu  <https://orcid.org/0000-0002-4323-5083>  
 Yi Zhang  <https://orcid.org/0000-0001-8738-1851>  
 Zhongliang Zu  <https://orcid.org/0000-0001-7361-7480>

## REFERENCES

- Zhou J, Payen J, Wilson DA, Traystman RJ, van Zijl PCM. Using the amide proton signals of intracellular proteins and peptides to detect pH effects in MRI. *Nature Med.* 2003;9:1085-1090.
- Zhou J, Lal B, Wilson DA, Larterra J, van Zijl PCM. Amide proton transfer (APT) contrast for imaging of brain tumors. *Magn Reson Med.* 2003;50:1120-1126.
- Ward KM, Aletras AH, Balaban RS. A new class of contrast agents for MRI based on proton chemical exchange dependent saturation transfer (CEST). *J Magn Reson.* 2000;143:79-87.
- Zhou J, van Zijl PC. Chemical exchange saturation transfer imaging and spectroscopy. *Progr NMR Spectr.* 2006;48:109-136.
- Sherry AD, Woods M. Chemical exchange saturation transfer contrast agents for magnetic resonance imaging. *Annu Rev Biomed Eng.* 2008;10:391-411.
- van Zijl PCM, Yadav NN. Chemical exchange saturation transfer (CEST): what is in a name and what isn't? *Magn Reson Med.* 2011;65:927-948.
- Zhou JY, van Zijl PCM. Defining an acidosis-based ischemic penumbra from pH-weighted MRI. *Transl Stroke Res.* 2012;3:76-83.
- Kogan F, Hariharan H, Reddy R. Chemical exchange saturation transfer (CEST) imaging: description of technique and potential clinical applications. *Curr Radiol Rep.* 2013;1:102-114.
- Liu G, Song X, Chan KW, McMahan MT. Nuts and bolts of chemical exchange saturation transfer MRI. *NMR Biomed.* 2013;26:810-828.
- Vinogradov E, Sherry AD, Lenkinski RE. CEST: from basic principles to applications, challenges and opportunities. *J Magn Reson.* 2013;229:155-172.
- Jones KM, Pollard AC, Pagel MD. Clinical applications of chemical exchange saturation transfer (CEST) MRI. *J Magn Reson Imaging.* 2018;47:11-27.
- Zhou J, Heo H-Y, Knutsson L, van Zijl PCM, Jiang S. APT-weighted MRI: techniques, current neuro applications, and challenging issues. *J Magn Reson Imaging.* 2019;50:347-364.
- Dou W, Lin CE, Ding H, et al. Chemical exchange saturation transfer magnetic resonance imaging and its main and potential applications in pre-clinical and clinical studies. *Quant Imaging Med Surg.* 2019;9:1747-1766.
- Kamimura K, Nakajo M, Yoneyama T, et al. Amide proton transfer imaging of tumors: theory, clinical applications, pitfalls, and future directions. *Jpn J Radiol.* 2019;37:109-116.
- Sotirios B, Demetriou E, Topriceanu CC, Zakrzewska Z. The role of APT imaging in gliomas grading: a systematic review and meta-analysis. *Eur J Radiol.* 2020;133:109353.

16. Consolino L, Anemone A, Capozza M, et al. Non-invasive investigation of tumor metabolism and acidosis by MRI-CEST imaging. *Front Oncol.* 2020;10:161.
17. Mamoune KE, Barantin L, Adriaensen H, Tillet Y. Application of chemical exchange saturation transfer (CEST) in neuroimaging. *J Chem Neuroanat.* 2021;114:101944.
18. Foo LS, Harston G, Mehndiratta A, et al. Clinical translation of amide proton transfer (APT) MRI for ischemic stroke: a systematic review (2003–2020). *Quant Imaging Med Surg.* 2021;11:3797-3811.
19. Kim H, Krishnamurthy LC, Sun PZ. Brain pH imaging and its applications. *Neuroscience.* 2021;474:51-62.
20. Zhang H, Zhou J, Peng Y. Amide proton transfer-weighted MR imaging of pediatric central nervous system diseases. *Magn Reson Imaging Clin N Am.* 2021;29:631-641.
21. Gao T, Zou C, Li Y, Jiang Z, Tang X, Song X. A brief history and future prospects of CEST MRI in clinical non-brain tumor imaging. *Int J Mol Sci.* 2021;22:11559. doi:10.3390/ijms222111559
22. Jones CK, Schlosser MJ, van Zijl PC, Pomper MG, Golay X, Zhou J. Amide proton transfer imaging of human brain tumors at 3T. *Magn Reson Med.* 2006;56:585-592.
23. Zhou J, Blakeley JO, Hua J, et al. Practical data acquisition method for human brain tumor amide proton transfer (APT) imaging. *Magn Reson Med.* 2008;60:842-849.
24. Wen Z, Hu S, Huang F, et al. MR imaging of high-grade brain tumors using endogenous protein and peptide-based contrast. *Neuroimage.* 2010;51:616-622.
25. Zhou J, Zhu H, Lim M, et al. Three-dimensional amide proton transfer MR imaging of gliomas: initial experience and comparison with gadolinium enhancement. *J Magn Reson Imaging.* 2013;38:1119-1128.
26. Togao O, Yoshiura T, Keupp J, et al. Amide proton transfer imaging of adult diffuse gliomas: correlation with histopathological grades. *Neuro Oncol.* 2014;16:441-448.
27. Sakata A, Okada T, Yamamoto A, et al. Grading glial tumors with amide proton transfer MR imaging: different analytical approaches. *J Neurooncol.* 2015;122:339-348.
28. Jiang S, Yu H, Wang X, et al. Molecular MRI differentiation between primary central nervous system lymphomas and high-grade gliomas using endogenous protein-based amide proton transfer MR imaging at 3 Tesla. *Eur Radiol.* 2016;26:64-71.
29. Jiang S, Eberhart CG, Zhang Y, et al. Amide proton transfer-weighted MR image-guided stereotactic biopsy in patients with newly diagnosed gliomas. *Eur J Cancer.* 2017;83:9-18.
30. Choi YS, Ahn SS, Lee SK, et al. Amide proton transfer imaging to discriminate between low- and high-grade gliomas: added value to apparent diffusion coefficient and relative cerebral blood volume. *Eur Radiol.* 2017;27:3181-3189.
31. Su C, Liu C, Zhao L, et al. Amide proton transfer imaging allows detection of glioma grades and tumor proliferation: comparison with Ki-67 expression and proton MR spectroscopy imaging. *AJNR Am J Neuroradiol.* 2017;38:1702-1709.
32. Bai Y, Lin Y, Zhang W, et al. Noninvasive amide proton transfer magnetic resonance imaging in evaluating the grading and cellularity of gliomas. *Oncotarget.* 2017;8:5834.
33. Zou T, Yu H, Jiang C, et al. Differentiating the histological grades of gliomas preoperatively using amide proton transfer-weighted (APTW) and intravoxel incoherent motion MRI. *NMR Biomed.* 2018;31:e3850.
34. Zhang J, Zhu W, Tain R, Zhou XJ, Cai K. Improved differentiation of low-grade and high-grade gliomas and detection of tumor proliferation using APT contrast fitted from Z-spectrum. *Mol Imaging Biol.* 2018;20:623-631.
35. Sun H, Xin J, Zhou J, Lu Z, Guo Q. Applying amide proton transfer MR imaging to hybrid brain PET/MR: concordance with gadolinium enhancement and added value to [(18)F]FDG PET. *Mol Imaging Biol.* 2018;20:473-481.
36. Schon S, Cabello J, Liesche-Starnecker F, et al. Imaging glioma biology: spatial comparison of amino acid PET, amide proton transfer, and perfusion-weighted MRI in newly diagnosed gliomas. *Eur J Nucl Med Mol Imaging.* 2020;47:1468-1475.
37. Durmo F, Rydhog A, Testud F, et al. Assessment of amide proton transfer weighted (APTw) MRI for pre-surgical prediction of final diagnosis in gliomas. *PLoS One.* 2020;15:e0244003.
38. Zhou J, Tryggstad E, Wen Z, et al. Differentiation between glioma and radiation necrosis using molecular magnetic resonance imaging of endogenous proteins and peptides. *Nature Med.* 2011;17:130-134.
39. Hong X, Liu L, Wang M, et al. Quantitative multiparametric MRI assessment of glioma response to radiotherapy in a rat model. *Neuro Oncol.* 2014;16:856-867.
40. Sagiya K, Mashimo T, Togao O, et al. In vivo chemical exchange saturation transfer imaging allows early detection of a therapeutic response in glioblastoma. *Proc Natl Acad Sci U S A.* 2014;111:4542-4547.
41. Ma B, Blakeley JO, Hong X, et al. Applying amide proton transfer-weighted MRI to distinguish pseudoprogression from true progression in malignant gliomas. *J Magn Reson Imaging.* 2016;44:456-462.
42. Park JE, Kim HS, Park KJ, Kim SJ, Kim JH, Smith SA. Pre- and posttreatment glioma: comparison of amide proton transfer imaging with MR spectroscopy for biomarkers of tumor proliferation. *Radiology.* 2016;278:514-523.
43. Jiang S, Eberhart CG, Lim M, et al. Identifying recurrent malignant glioma after treatment using amide proton transfer-weighted MR imaging: a validation study with image-guided stereotactic biopsy. *Clin Cancer Res.* 2019;25:552-561.
44. Park JE, Kim HS, Park SY, Jung SC, Kim JH, Heo HY. Identification of early response to anti-angiogenic therapy in recurrent glioblastoma: amide proton transfer-weighted and perfusion-weighted MRI compared with diffusion-weighted MRI. *Radiology.* 2020;295:397-406.
45. Liu J, Li C, Chen Y, et al. Diagnostic performance of multiparametric MRI in the evaluation of treatment response in glioma patients at 3T. *J Magn Reson Imaging.* 2020;51:1154-1161.
46. Regnery S, Adeberg S, Dreher C, et al. Chemical exchange saturation transfer MRI serves as predictor of early progression in glioblastoma patients. *Oncotarget.* 2018;9:28772-28783.
47. Paech D, Dreher C, Regnery S, et al. Relaxation-compensated amide proton transfer (APT) MRI signal intensity is associated with survival and progression in high-grade glioma patients. *Eur Radiol.* 2019;29:4957-4967.
48. Joo B, Han K, Ahn SS, et al. Amide proton transfer imaging might predict survival and IDH mutation status in high-grade glioma. *Eur Radiol.* 2019;29:6643-6652.



49. Jiang S, Zou T, Eberhart CG, et al. Predicting IDH mutation status in grade II gliomas using amide proton transfer-weighted (APT<sub>w</sub>) MRI. *Magn Reson Med*. 2017;78:1100-1109.
50. Jiang S, Rui Q, Wang Y, et al. Discriminating MGMT promoter methylation status in patients with glioblastoma employing amide proton transfer-weighted MRI metrics. *Eur Radiol*. 2018;28:2115-2123.
51. Su L, Gao P, Lin S, et al. Predicting O6-methylguanine-DNA methyltransferase protein expression in primary low- and high-grade gliomas using certain qualitative characteristics of amide proton transfer-weighted magnetic resonance imaging. *World Neurosurg*. 2018;116:E814-E823.
52. Paech D, Windschuh J, Oberhollenzer J, et al. Assessing the predictability of IDH mutation and MGMT methylation status in glioma patients using relaxation-compensated multi-pool CEST MRI at 7.0 Tesla. *Neuro-Oncol*. 2018;20:1661-1671.
53. Han Y, Wang W, Yang Y, et al. Amide proton transfer imaging in predicting isocitrate dehydrogenase 1 mutation status of grade II/III gliomas based on support vector machine. *Front Neurosci*. 2020;14:144.
54. Xu Z, Ke C, Liu J, et al. Diagnostic performance between MR amide proton transfer (APT) and diffusion kurtosis imaging (DKI) in glioma grading and IDH mutation status prediction at 3T. *Eur J Radiol*. 2021;134:109466.
55. Zhuo Z, Qu L, Zhang P, et al. Prediction of H3K27M-mutant brainstem glioma by amide proton transfer-weighted imaging and its derived radiomics. *Eur J Nucl Med Mol Imaging*. 2021;48:4426-4436.
56. Mancini L, Casagrande S, Gautier G, et al. CEST MRI provides amide/amine surrogate biomarkers for treatment-naïve glioma sub-typing. *Eur J Nucl Med Mol Imaging*. 2022. doi:10.1007/s00259-00022-05676-00251
57. Weinreb JC, Rodby RA, Yee J, et al. Use of intravenous gadolinium-based contrast media in patients with kidney disease: consensus statements from the American College of Radiology and the National Kidney Foundation. *Radiology*. 2021;298:28-35.
58. Woolen SA, Shankar PR, Gagnier JJ, MacEachern MP, Singer L, Davenport MS. Risk of nephrogenic systemic fibrosis in patients with stage 4 or 5 chronic kidney disease receiving a group II gadolinium-based contrast agent: a systematic review and meta-analysis. *JAMA Intern Med*. 2020;180:223-230.
59. Kanda T, Fukusato T, Matsuda M, et al. Gadolinium-based contrast agent accumulates in the brain even in subjects without severe renal dysfunction: evaluation of autopsy brain specimens with inductively coupled plasma mass spectroscopy. *Radiology*. 2015;276:228-232.
60. 3D APT U.S. Food and Drug Administration web site. [https://www.accessdata.fda.gov/cdrh\\_docs/pdf17/K172920.pdf](https://www.accessdata.fda.gov/cdrh_docs/pdf17/K172920.pdf). Published January 22, 2018.
61. van de Ven K & Keupp J Amide proton transfer weighted imaging: Advancement in molecular tumor diagnosis. [http://images.philips.com/is/content/PhilipsConsumer/Campaigns/HC20140401\\_DG/HC-Master-White\\_paper\\_3D\\_APT\\_14062018.PDF](http://images.philips.com/is/content/PhilipsConsumer/Campaigns/HC20140401_DG/HC-Master-White_paper_3D_APT_14062018.PDF). Published June 2018.
62. The 7th International Workshop on Chemical Exchange Saturation Transfer (CEST) Imaging web site. <http://cest2018.medmeeting.org>.
63. The 8th International Workshop on Chemical Exchange Saturation Transfer (CEST) Imaging web site. <https://www.cestworkshop.org/>.
64. Zhou J, Wilson DA, Sun PZ, Klaus JA, van Zijl PCM. Quantitative description of proton exchange processes between water and endogenous and exogenous agents for WEX, CEST, and APT experiments. *Magn Reson Med*. 2004;51:945-952.
65. Sun PZ, Zhou J, Huang J, van Zijl P. Simplified quantitative description of amide proton transfer (APT) imaging during acute ischemia. *Magn Reson Med*. 2007;57:405-410.
66. Jin T, Wang P, Zong XP, Kim SG. Magnetic resonance imaging of the amine-proton EXchange (APEX) dependent contrast. *Neuroimage*. 2012;59:1218-1227.
67. Zaiss M, Bachert P. Chemical exchange saturation transfer (CEST) and MR Z-spectroscopy in vivo: a review of theoretical approaches and methods. *Phys Med Biol*. 2013;58:R221-R269.
68. Kim J, Wu Y, Guo Y, Zheng H, Sun PZ. A review of optimization and quantification techniques for chemical exchange saturation transfer MRI toward sensitive in vivo imaging. *Contrast Media Mol Imaging*. 2015;10:163-178.
69. Chappell MA, Donahue MJ, Tee YK, et al. Quantitative Bayesian model-based analysis of amide proton transfer MRI. *Magn Reson Med*. 2013;70:556-567.
70. Cohen O, Huang S, McMahon MT, Rosen MS, Farrar CT. Rapid and quantitative chemical exchange saturation transfer (CEST) imaging with magnetic resonance fingerprinting (MRF). *Magn Reson Med*. 2018;80:2449-2463.
71. Heo HY, Han Z, Jiang S, Schar M, van Zijl PCM, Zhou J. Quantifying amide proton exchange rate and concentration in chemical exchange saturation transfer imaging of the human brain. *Neuroimage*. 2019;189:202-213.
72. Henkelman RM, Stanisz GJ, Graham SJ. Magnetization transfer in MRI: a review. *NMR Biomed*. 2001;14:57-64.
73. Ling W, Regatte RR, Navon G, Jerschow A. Assessment of glycosaminoglycan concentration in vivo by chemical exchange-dependent saturation transfer (gagCEST). *Proc Natl Acad Sci U S A*. 2008;105:2266-2270.
74. Jones CK, Huang A, Xu J, et al. Nuclear Overhauser enhancement (NOE) imaging in the human brain at 7T. *Neuroimage*. 2013;77:114-124.
75. Jin T, Wang P, Zong X, Kim S-G. MR imaging of the amide-proton transfer effect and the pH-insensitive nuclear overhauser effect at 9.4 T. *Magn Reson Med*. 2013;69:760-770.
76. Hua J, Jones CK, Blakeley J, Smith SA, van Zijl PCM, Zhou J. Quantitative description of the asymmetry in magnetization transfer effects around the water resonance in the human brain. *Magn Reson Med*. 2007;58:786-793.
77. van Zijl PCM, Lam WW, Xu J, Knutsson L, Stanisz GJ. Magnetization transfer contrast and chemical exchange saturation transfer MRI. Features and analysis of the field-dependent saturation spectrum. *Neuroimage*. 2018;168:222-241.
78. Mori S, Eleff SM, Pilatus U, Mori N, van Zijl PCM. Proton NMR spectroscopy of solvent-saturable resonance: a new approach to study pH effects *in situ*. *Magn Reson Med*. 1998;40:36-42.
79. van Zijl PCM, Zhou J, Mori N, Payen J, Mori S. Mechanism of magnetization transfer during on-resonance water saturation. A new approach to detect mobile proteins, peptides, and lipids. *Magn Reson Med*. 2003;49:440-449.

80. Maintz D, Heindel W, Kugel H, Jaeger R, Lackner KJ. Phosphorus-31 MR spectroscopy of normal adult human brain and brain tumors. *NMR Biomed.* 2002;15:18-27.
81. Wenger KJ, Hattingen E, Franz K, Steinbach JP, Bahr O, Pilatus U. Intracellular pH measured by (31) P-MR-spectroscopy might predict site of progression in recurrent glioblastoma under antiangiogenic therapy. *J Magn Reson Imaging.* 2017;46:1200-1208.
82. Walchhofer LM, Steiger R, Rietzler A, et al. Phosphorous magnetic resonance spectroscopy to detect regional differences of energy and membrane metabolism in naive glioblastoma Multiforme. *Cancer.* 2021;13:2598.
83. Yan K, Fu Z, Yang C, et al. Assessing amide proton transfer (APT) MRI contrast origins in 9L gliosarcoma in the rat brain using proteomic analysis. *Mol Imaging Biol.* 2015;17:479-487.
84. Lee DH, Heo HY, Zhang K, et al. Quantitative assessment of the effects of water proton concentration and water T1 changes on amide proton transfer (APT) and nuclear overhauser enhancement (NOE) MRI: the origin of the APT imaging signal in brain tumor. *Magn Reson Med.* 2017;77:855-863.
85. Schure JR, Shrestha M, Breuer S, et al. The pH sensitivity of APT-CEST using phosphorus spectroscopy as a reference method. *NMR Biomed.* 2019;32:e4125.
86. Ray KJ, Simard MA, Larkin JR, et al. Tumor pH and protein concentration contribute to the signal of amide proton transfer magnetic resonance imaging. *Cancer Res.* 2019;79:1343-1352.
87. Hobbs SK, Shi G, Homer R, Harsh G, Altias SW, Bednarski MD. Magnetic resonance imaging-guided proteomics of human glioblastoma multiforme. *J Magn Reson Imaging.* 2003;18:530-536.
88. Li J, Zhuang Z, Okamoto H, et al. Proteomic profiling distinguishes astrocytomas and identifies differential tumor markers. *Neurology.* 2006;66:733-736.
89. Howe FA, Barton SJ, Cudlip SA, et al. Metabolic profiles of human brain tumors using quantitative in vivo <sup>1</sup>H magnetic resonance spectroscopy. *Magn Reson Med.* 2003;49:223-232.
90. Griffiths JR. Are cancer cells acidic? *Br J Cancer.* 1991;64:425-427.
91. Gillies RJ, Raghunand N, Karczmar GS, Bhujwala ZM. MRI of the tumor microenvironment. *J Magn Reson Imaging.* 2002;16:430-450.
92. Lindeman LR, Randtke EA, High RA, Jones KM, Howison CM, Pagel MD. A comparison of exogenous and endogenous CEST MRI methods for evaluating in vivo pH. *Magn Reson Med.* 2018;79:2766-2772.
93. Hua J, van Zijl PCM, Sun PZ, Zhou J. Quantitative description of magnetization transfer (MT) asymmetry in experimental brain tumors. *Proc 15th Annual Meeting ISMRM;* 2007:882.
94. Zhou J, Hong X, Zhao X, Gao J-H, Yuan J. APT-weighted and NOE-weighted image contrasts in glioma with different RF saturation powers based on magnetization transfer ratio asymmetry analyses. *Magn Reson Med.* 2013;70:320-327.
95. Heo HY, Zhang Y, Lee DH, Hong X, Zhou J. Quantitative assessment of amide proton transfer (APT) and nuclear overhauser enhancement (NOE) imaging with extrapolated semi-solid magnetization transfer reference (EMR) signals: application to a rat glioma model at 4.7 Tesla. *Magn Reson Med.* 2016;75:137-149.
96. Heo HY, Zhang Y, Jiang S, Lee DH, Zhou J. Quantitative assessment of amide proton transfer (APT) and nuclear overhauser enhancement (NOE) imaging with extrapolated semisolid magnetization transfer reference (EMR) signals: II. Comparison of three EMR models and application to human brain glioma at 3 tesla. *Magn Reson Med.* 2016;75:1630-1639.
97. Jin T, Kim S-G. In vivo saturation transfer imaging of nuclear overhauser effect from aromatic and aliphatic protons: implication to APT quantification. *Proc 21th Annual Meeting ISMRM;* 2013:2528.
98. Zaiss M, Windschuh J, Goerke S, et al. Downfield-NOE-suppressed amide-CEST-MRI at 7 tesla provides a unique contrast in human glioblastoma. *Magn Reson Med.* 2017;77:196-208.
99. Zu Z. Towards the complex dependence of MTR<sub>asym</sub> on T1w in amide proton transfer (APT) imaging. *NMR Biomed.* 2018;31:e3934.
100. Heo HY, Lee DH, Zhang Y, et al. Insight into the quantitative metrics of chemical exchange saturation transfer (CEST) imaging. *Magn Reson Med.* 2017;77:1853-1865.
101. Xu J, Zaiss M, Zu Z, et al. On the origins of chemical exchange saturation transfer (CEST) contrast in tumors at 9.4 T. *NMR Biomed.* 2014;27:406-416.
102. Zaiss M, Windschuh J, Paech D, et al. Relaxation-compensated CEST-MRI of the human brain at 7T: unbiased insight into NOE and amide signal changes in human glioblastoma. *Neuroimage.* 2015;112:180-188.
103. Tee YK, Donahue MJ, Harston GW, Payne SJ, Chappell MA. Quantification of amide proton transfer effect pre- and post-gadolinium contrast agent administration. *J Magn Reson Imaging.* 2014;40:832-838.
104. Harris RJ, Cloughesy TF, Liau LM, et al. pH-weighted molecular imaging of gliomas using amine chemical exchange saturation transfer MRI. *Neuro-Oncol.* 2015;17:1514-1524.
105. Haris M, Nanga RPR, Singh A, et al. Exchange rates of creatine kinase metabolites: feasibility of imaging creatine by chemical exchange saturation transfer MRI. *NMR Biomed.* 2012;25:1305-1309.
106. Khlebnikov V, van der Kemp WJM, Hoogduin H, Klomp DWJ, Prompers JJ. Analysis of chemical exchange saturation transfer contributions from brain metabolites to the Z-spectra at various field strengths and pH. *Sci Rep.* 2019;9:1089.
107. Cai K, Singh A, Poptani H, et al. CEST signal at 2ppm (CEST@2ppm) from Z-spectral fitting correlates with creatine distribution in brain tumor. *NMR Biomed.* 2015;28:1-8.
108. Su C, Xu S, Lin D, et al. Multi-parametric Z-spectral MRI may have a good performance for glioma stratification in clinical patients. *Eur Radiol.* 2021;32:101-111. doi:10.1007/s00330-00021-08175-3
109. Zaiss M, Kunz P, Goerke S, Radbruch A, Bachert P. MR imaging of protein folding in vitro employing nuclear-Overhauser-mediated saturation transfer. *NMR Biomed.* 2013;26:1815-1822.
110. Goerke S, Zaiss M, Kunz P, et al. Signature of protein unfolding in chemical exchange saturation transfer imaging. *NMR Biomed.* 2015;28:906-913.
111. Keupp J, Togao O. Magnetization transfer ratio based metric for APTw or CESTw MRI suppressing signal from fluid compartments - initial application to glioblastoma assessment. *Proc 26th Annual Meeting ISMRM;* 2018:3156.
112. Wang M, Hong X, Chang CF, et al. Simultaneous detection and separation of hyperacute intracerebral hemorrhage and

- cerebral ischemia using amide proton transfer MRI. *Magn Reson Med.* 2015;74:42-50.
113. Grossman R, Tyler B, Brem H, et al. Growth properties of SF188/V+ human glioma in rats in vivo observed by magnetic resonance imaging. *J Neurooncol.* 2012;110:315-323.
  114. Jeong HK, Han K, Zhou J, et al. Characterizing amide proton transfer imaging in haemorrhage brain lesions using 3T MRI. *Eur Radiol.* 2017;27:1577-1584.
  115. Ma X, Bai Y, Lin Y, et al. Amide proton transfer magnetic resonance imaging in detecting intracranial hemorrhage at different stages: a comparative study with susceptibility weighted imaging. *Sci Rep.* 2017;7:45696.
  116. van Zijl PCM, Sehgal AA. Proton chemical exchange saturation transfer (CEST) MRS and MRI. *Emagres.* 2016;5:1307-1332.
  117. Ji Y, Zhou IY, Qiu BS, Sun PZ. Progress toward quantitative in vivo chemical exchange saturation transfer (CEST) MRI. *Isr J Chem.* 2017;57:809-824.
  118. Badve C, Yu A, Dastmalchian S, et al. MR fingerprinting of adult brain tumors: initial experience. *AJNR Am J Neuroradiol.* 2017;38:492-499.
  119. Zhang Y, Liu X, Zhou J, Bottomley PA. Ultrafast compartmentalized relaxation time mapping with linear algebraic modeling. *Magn Reson Med.* 2018;79:286-297.
  120. Togao O, Hiwatashi A, Keupp J, et al. Amide proton transfer imaging of diffuse gliomas: effect of saturation pulse length in parallel transmission-based technique. *PLoS One.* 2016;11:e0155925.
  121. Scheidegger R, Vinogradov E, Alsop DC. Amide proton transfer imaging with improved robustness to magnetic field inhomogeneity and magnetization transfer asymmetry using saturation with frequency alternating RF irradiation. *Magn Reson Med.* 2011;66:1275-1285.
  122. Zhu H, Jones CK, van Zijl PCM, Barker PB, Zhou J. Fast 3D chemical exchange saturation transfer (CEST) imaging of the human brain. *Magn Reson Med.* 2010;64:638-644.
  123. Jia G, Abaza R, Williams JD, et al. Amide proton transfer MR imaging of prostate cancer: a preliminary study. *J Magn Reson Imaging.* 2011;33:647-654.
  124. Dula AN, Arlinghaus LR, Dortch RD, et al. Amide proton transfer imaging of the breast at 3 T: establishing reproducibility and possible feasibility assessing chemotherapy response. *Magn Reson Med.* 2013;70:216-224.
  125. Sun PZ, Benner T, Kumar A, Sorensen AG. Investigation of optimizing and translating pH-sensitive pulsed-chemical exchange saturation transfer (CEST) imaging to a 3T clinical scanner. *Magn Reson Med.* 2008;60:834-841.
  126. Schmitt B, Zaiß M, Zhou J, Bachert P. Optimization of pulse train presaturation for CEST imaging in clinical scanners. *Magn Reson Med.* 2011;65:1620-1629.
  127. Tee YK, Harston GW, Blockley N, et al. Comparing different analysis methods for quantifying the MRI amide proton transfer (APT) effect in hyperacute stroke patients. *NMR Biomed.* 2014;27:1019-1029.
  128. Ohno Y, Yui M, Koyama H, et al. Chemical exchange saturation transfer MR imaging: preliminary results for differentiation of malignant and benign thoracic lesions. *Radiology.* 2016;279:578-589.
  129. Herz K, Mueller S, Perlman O, et al. Pulseseq-CEST: towards multi-site multi-vendor compatibility and reproducibility of CEST experiments using an open source sequence standard. *Magn Reson Med.* 2021;86:1845-1858.
  130. Keupp J, Balthes C, Harvey PR, van den Brink J. Parallel RF transmission based MRI technique for highly sensitive detection of amide proton transfer in the human brain. *Proc 19th Annual Meeting ISMRM;* 2011:710.
  131. Zhu H, Keupp J, Blakeley J, et al. Interleaved parallel transmission saturation scheme for 3D amide proton transfer imaging of brain tumors at 3 Tesla. *Proc 20th Annual Meeting ISMRM;* 2012:743.
  132. Dixon WT, Hancu I, Ratnakar SJ, Sherry AD, Lenkinski RE, Alsop DC. A multislice gradient echo pulse sequence for CEST imaging. *Magn Reson Med.* 2010;63:253-256.
  133. Dula AN, Asche EM, Landman BA, et al. Development of chemical exchange saturation transfer at 7T. *Magn Reson Med.* 2011;66:831-838.
  134. Jones CK, Polders D, Hua J, et al. In vivo 3D whole-brain pulsed steady state chemical exchange saturation transfer at 7T. *Magn Reson Med.* 2012;67:1579-1589.
  135. Smith SA, Farrell JA, Jones CK, Reich DS, Calabresi PA, van Zijl PC. Pulsed magnetization transfer imaging with body coil transmission at 3 tesla: feasibility and application. *Magn Reson Med.* 2006;56:866-875.
  136. Park JE, Kim HS, Park KJ, Choi CG, Kim SJ. Histogram analysis of amide proton transfer imaging to identify contrast-enhancing low-grade brain tumor that mimics high-grade tumor: increased accuracy of MR perfusion. *Radiology.* 2015;277:151-161.
  137. Yoshimaru ES, Randtke EA, Pagel MD, Cardenas-Rodriguez J. Design and optimization of pulsed chemical exchange saturation transfer MRI using a multiobjective genetic algorithm. *J Magn Reson.* 2016;263:184-192.
  138. Lin EC, Li H, Zu Z, et al. Chemical exchange rotation transfer (CERT) on human brain at 3 tesla. *Magn Reson Med.* 2018;80:2609-2617.
  139. Kim B, So S, Park H. Optimization of steady-state pulsed CEST imaging for amide proton transfer at 3T MRI. *Magn Reson Med.* 2019;81:3616-3627.
  140. Lee H, Choi SH, Sohn CH, Kim SG, Lee J, Park J. Rapid three-dimensional steady-state chemical exchange saturation transfer magnetic resonance imaging. *Magn Reson Med.* 2021;85:1209-1221.
  141. Warnert EAH, Wood TC, Incekara F, et al. Mapping tumour heterogeneity with pulsed 3D CEST MRI in non-enhancing glioma at 3 T. *Magma.* 2021;35:53-62.
  142. Zhao X, Wen Z, Huang F, et al. Saturation power dependence of amide proton transfer image contrasts in human brain tumors and strokes at 3 T. *Magn Reson Med.* 2011;66:1033-1041.
  143. Herz K, Zaiss M. Pulseseq-cest-library. GitHub web site. <https://pulseseq-cest.github.io/>. Accessed December 2021.
  144. Sun PZ, Zhou J, Sun W, Huang J, van Zijl PC. Suppression of lipid artifacts in amide proton transfer (APT) imaging. *Magn Reson Med.* 2005;54:222-225.
  145. Zhang S, Seiler S, Wang X, et al. CEST-Dixon for human breast lesion characterization at 3 T: a preliminary study. *Magn Reson Med.* 2018;80:895-903.
  146. Zhao Y, Yan X, Zhang Z, Zhao W, Liu Z, Li J. Self-adapting multi-peak water-fat reconstruction for the removal of lipid

- artifacts in chemical exchange saturation transfer (CEST) imaging. *Magn Reson Med.* 2019;82:1700-1712.
147. Zimmermann F, Korzowski A, Breitling J, et al. A novel normalization for amide proton transfer CEST MRI to correct for fat signal-induced artifacts: application to human breast cancer imaging. *Magn Reson Med.* 2020;83:920-934.
  148. Zhang Y, Heo HY, Jiang S, Zhou J, Bottomley PA. Fast 3D chemical exchange saturation transfer imaging with variably-accelerated sensitivity encoding (vSENSE). *Magn Reson Med.* 2019;82:2046-2061.
  149. Zhang Y, Yong X, Liu R, et al. Whole-brain chemical exchange saturation transfer imaging with optimized turbo spin echo readout. *Magn Reson Med.* 2020;84:1161-1172.
  150. Sun PZ, Murata Y, Lu J, Wang X, Lo EH, Sorensen AG. Relaxation-compensated fast multislice amide proton transfer (APT) imaging of acute ischemic stroke. *Magn Reson Med.* 2008;59:1175-1182.
  151. Debnath A, Gupta RK, Reddy R, Singh A. Effect of offset-frequency step size and interpolation methods on chemical exchange saturation transfer MRI computation in human brain. *NMR Biomed.* 2021;34:e4468.
  152. Pruessmann KP, Weiger M, Scheidegger MB, Boesiger P. SENSE: sensitivity encoding for fast MRI. *Magn Reson Med.* 1999;42:952-962.
  153. Zhang Y, Heo HY, Lee DH, et al. Chemical exchange saturation transfer (CEST) imaging with fast variably-accelerated sensitivity encoding (vSENSE). *Magn Reson Med.* 2017;77:2225-2238.
  154. Griswold MA, Jakob PM, Heidemann RM, et al. Generalized autocalibrating partially parallel acquisitions (GRAPPA). *Magn Reson Med.* 2002;47:1202-1210.
  155. Breuer FA, Blaimer M, Heidemann RM, Mueller MF, Griswold MA, Jakob PM. Controlled aliasing in parallel imaging results in higher acceleration (CAIPIRINHA) for multi-slice imaging. *Magn Reson Med.* 2005;53:684-691.
  156. Zhao X, Wen Z, Zhang G, et al. Three-dimensional turbo-spin-echo amide proton transfer MR imaging at 3-tesla and its application to high-grade human brain tumors. *Mol Imaging Biol.* 2013;15:114-122.
  157. Zaiss M, Ehse P, Scheffler K. Snapshot-CEST: optimizing spiral-centric-reordered gradient echo acquisition for fast and robust 3D CEST MRI at 9.4 T. *NMR Biomed.* 2018;31:e3879.
  158. Deshmane A, Zaiss M, Lindig T, et al. 3D gradient echo snapshot CEST MRI with low power saturation for human studies at 3T. *Magn Reson Med.* 2019;81:2412-2423.
  159. Mueller S, Stirnberg R, Akbey S, et al. Whole brain snapshot CEST at 3T using 3D-EPI: aiming for speed, volume, and homogeneity. *Magn Reson Med.* 2020;84:2469-2483.
  160. Varma G, Lenkinski R, Vinogradov E. Keyhole chemical exchange saturation transfer. *Magn Reson Med.* 2012;68:1228-1233.
  161. Zhang Y, Heo HY, Jiang S, Lee DH, Bottomley PA, Zhou J. Highly accelerated chemical exchange saturation transfer (CEST) measurements with linear algebraic modeling. *Magn Reson Med.* 2016;76:136-144.
  162. Heo HY, Zhang Y, Lee DH, Jiang S, Zhao X, Zhou J. Accelerating chemical exchange saturation transfer (CEST) MRI by combining compressed sensing and sensitivity encoding techniques. *Magn Reson Med.* 2017;77:779-786.
  163. She H, Greer JS, Zhang S, et al. Accelerating chemical exchange saturation transfer MRI with parallel blind compressed sensing. *Magn Reson Med.* 2019;81:504-513.
  164. Heo HY, Xu X, Jiang S, et al. Prospective acceleration of parallel RF transmission-based 3D chemical exchange saturation transfer imaging with compressed sensing. *Magn Reson Med.* 2019;82:1812-1821.
  165. Wang P, Guo P, Lu J, Zhou J, Jiang S, Patel VM. Improving amide proton transfer-weighted MRI reconstruction using T2-weighted images. *Medical Image Computing and Computer Assisted Intervention - MICCAI 2020*; 2020:3-12.
  166. Kim M, Gillen J, Landman BA, Zhou J, van Zijl PCM. Water saturation shift referencing (WASSR) for chemical exchange saturation transfer (CEST) experiments. *Magn Reson Med.* 2009;61:1441-1450.
  167. Wei W, Jia G, Flanigan D, Zhou J, Knopp MV. Chemical exchange saturation transfer MR imaging of articular cartilage glycosaminoglycans at 3 T: accuracy of B<sub>0</sub> field inhomogeneity corrections with gradient echo method. *Magn Reson Imaging.* 2014;32:41-47.
  168. Schmidt H, Schwenzer NF, Gatidis S, et al. Systematic evaluation of amide proton chemical exchange saturation transfer at 3T: effects of protein concentration, pH, and acquisition parameters. *Invest Radiol.* 2016;51:635-646.
  169. Keupp J, Eggers H. CEST-Dixon MRI for sensitive and accurate measurement of amide proton transfer in humans at 3T. *Proc 18th Annual Meeting ISMRM*; 2010:338.
  170. Togao O, Keupp J, Hiwatashi A, et al. Amide proton transfer imaging of brain tumors using a self-corrected 3D fast spin-echo dixon method: comparison with separate B<sub>0</sub> correction. *Magn Reson Med.* 2017;77:2272-2279.
  171. Schuenke P, Windschuh J, Roeloffs V, Ladd ME, Bachert P, Zaiss M. Simultaneous mapping of water shift and B1 (WASABI)-application to field-inhomogeneity correction of CEST MRI data. *Magn Reson Med.* 2017;77:571-580.
  172. Simegn GL, Van der Kouwe AJW, Robertson FC, Meintjes EM, Alhamud A. Real-time simultaneous shim and motion measurement and correction in glycoCEST MRI using double volumetric navigators (DvNavs). *Magn Reson Med.* 2019;81:2600-2613.
  173. Simegn GL, Alhamud A, van der Kouwe AJW, Meintjes E, Robertson F. Repeatability and reproducibility of prospective motion- and shim corrected 2D glycoCEST MRI. *Quant Imaging Med Surg.* 2019;9:1674-1685.
  174. Liu R, Zhang H, Niu W, et al. Improved chemical exchange saturation transfer imaging with real-time frequency drift correction. *Magn Reson Med.* 2019;81:2915-2923.
  175. Liu R, Zhang H, Qian Y, et al. Frequency-stabilized chemical exchange saturation transfer imaging with real-time free-induction-decay readout. *Magn Reson Med.* 2021;85:1322-1334.
  176. Windschuh J, Zaiss M, Ehse P, Lee JS, Jerschow A, Regatte RR. Assessment of frequency drift on CEST MRI and dynamic correction: application to gagCEST at 7 T. *Magn Reson Med.* 2019;81:573-582.
  177. Poblador Rodriguez E, Moser P, Dymerska B, et al. A comparison of static and dynamic B<sub>0</sub> mapping methods for correction of CEST MRI in the presence of temporal B<sub>0</sub> field variations. *Magn Reson Med.* 2019;82:633-646.

178. Li Y, Xie D, Cember A, et al. Accelerating GluCEST imaging using deep learning for B0 correction. *Magn Reson Med.* 2020;84:1724-1733.
179. Guivel-Scharen V, Sinnwell T, Wolff SD, Balaban RS. Detection of proton chemical exchange between metabolites and water in biological tissues. *J Magn Reson.* 1998;133:36-45.
180. Zaiss M, Schmitt B, Bachert P. Quantitative separation of CEST effect from magnetization transfer and spillover effects by Lorentzian-line-fit analysis of z-spectra. *J Magn Reson.* 2011;211:149-155.
181. Desmond KL, Moosvi F, Stanisz GJ. Mapping of amide, amine, and aliphatic peaks in the CEST spectra of murine xenografts at 7 T. *Magn Reson Med.* 2014;71:1841-1853.
182. Goerke S, Breitling J, Korzowski A, et al. Clinical routine acquisition protocol for 3D relaxation-compensated APT and rNOE CEST-MRI of the human brain at 3T. *Magn Reson Med.* 2021;86:393-404.
183. Tee YK, Khrapitchev AA, Sibson NR, Payne SJ, Chappell MA. Evaluating the use of a continuous approximation for model-based quantification of pulsed chemical exchange saturation transfer (CEST). *J Magn Reson.* 2012;222:88-95.
184. Liu D, Zhou J, Xue R, Zuo Z, An J, Wang DJJ. Quantitative characterization of nuclear Overhauser enhancement and amide proton transfer effects in the human brain at 7 Tesla. *Magn Reson Med.* 2013;70:1070-1081.
185. Sun PZ. Quasi-steady state chemical exchange saturation transfer (QUASS CEST) analysis-correction of the finite relaxation delay and saturation time for robust CEST measurement. *Magn Reson Med.* 2021;85:3281-3289.
186. Zhang XY, Zhai Y, Jin Z, Li C, Sun PZ, Wu Y. Preliminary demonstration of in vivo quasi-steady-state CEST postprocessing-correction of saturation time and relaxation delay for robust quantification of tumor MT and APT effects. *Magn Reson Med.* 2021;86:943-953.
187. Harris Geospatial Solutions web site. <https://www.l3harrisgeospatial.com/docs/loadingdefaultcolortables.html>. Accessed February 2022.
188. Chaffin M. IDL-Colorbars/IDL\_rgb\_values/013\_RAINBOW.dat. GitHub web site. [https://github.com/planetarmike/IDL-Colorbars/blob/master/IDL\\_rgb\\_values/013\\_RAINBOW.dat](https://github.com/planetarmike/IDL-Colorbars/blob/master/IDL_rgb_values/013_RAINBOW.dat). Accessed February 2022.
189. Borland D, Taylor MR 2nd. Rainbow color map (still) considered harmful. *IEEE Comput Graph Appl.* 2007;27:14-17.
190. Zaiss M, Herz K, Deshmane A, et al. Possible artifacts in dynamic CEST MRI due to motion and field alterations. *J Magn Reson.* 2019;298:16-22.
191. Li H, Li K, Zhang XY, et al. R1 correction in amide proton transfer imaging: indication of the influence of transcytolemmal water exchange on CEST measurements. *NMR Biomed.* 2015;28:1655-1662.
192. Quantitative imaging biomarkers alliance. The Radiological Society of North America (RSNA) web site. <https://www.rsna.org/research/quantitative-imaging-biomarkers-alliance>.
193. Paech D, Zaiss M, Meissner JE, et al. Nuclear Overhauser enhancement mediated chemical exchange saturation transfer imaging at 7 Tesla in glioblastoma patients. *PLoS One.* 2014;9:e104181.
194. Heo HY, Jones CK, Hua J, et al. Whole-brain amide proton transfer (APT) and nuclear overhauser enhancement (NOE) imaging in glioma patients using low-power steady-state pulsed chemical exchange saturation transfer (CEST) imaging at 7T. *J Magn Reson Imaging.* 2016;44:41-50.
195. Chan RW, Chen H, Myrehaug S, et al. Quantitative CEST and MT at 1.5T for monitoring treatment response in glioblastoma: early and late tumor progression during chemoradiation. *J Neurooncol.* 2021;151:267-278.
196. Chan RW, Lawrence LSP, Oglesby RT, et al. Chemical exchange saturation transfer MRI in central nervous system tumours on a 1.5 T MR-Linac. *Radiother Oncol.* 2021;162:140-149.
197. Salhotra A, Lal B, Laterra J, Sun PZ, van Zijl PCM, Zhou J. Amide proton transfer imaging of 9L gliosarcoma and human glioblastoma xenografts. *NMR Biomed.* 2008;21:489-497.
198. Su C, Zhao L, Li S, et al. Amid proton transfer (APT) and magnetization transfer (MT) MRI contrasts provide complementary assessment of brain tumors similarly to proton magnetic resonance spectroscopy imaging (MRSI). *Eur Radiol.* 2019;29:1203-1210.
199. Scheidegger R, Wong ET, Alsop DC. Contributors to contrast between glioma and brain tissue in chemical exchange saturation transfer sensitive imaging at 3 tesla. *Neuroimage.* 2014;99:256-268.
200. Miyoshi M, Matsuda T, Kabasawa H. CEST imaging with phase cycled rectangular RF preparation pulse: analytical solution, simulation and phantom study. *Proc 22th Annual Meeting ISMRM;* 2014:3299.
201. Lin G, Zhuang C, Shen Z, et al. APT weighted MRI as an effective imaging protocol to predict clinical outcome after acute ischemic stroke. *Front Neurol.* 2018;9:901.
202. Mehrabian H, Desmond KL, Soliman H, Sahgal A, Stanisz GJ. Differentiation between radiation necrosis and tumor progression using chemical exchange saturation transfer. *Clin Cancer Res.* 2017;23:3667-3675.
203. Goerke S, Soehngen Y, Deshmane A, et al. Relaxation-compensated APT and rNOE CEST-MRI of human brain tumors at 3 T. *Magn Reson Med.* 2019;82:622-632.

**How to cite this article:** Zhou J, Zaiss M, Knutsson L, et al. Review and consensus recommendations on clinical APT-weighted imaging approaches at 3T: Application to brain tumors. *Magn Reson Med.* 2022;88:546-574. doi: 10.1002/mrm.29241